Journal of Fluids and Structures 112 (2022) 103607

Contents lists available at ScienceDirect

Journal of Fluids and Structures

journal homepage: www.elsevier.com/locate/jfs

Optimized parametric hydrodynamic databases provide accurate response predictions and describe the physics of vortex-induced vibrations

Samuel Rudy [a,1], Dixia Fan [a,b,c,d,1], Jose del Aguila Ferrandis [a,b], Themistoklis P. Sapsis [a], Michael S. Triantafyllou [a,b,*]

[a] *Department of Mechanical Engineering, Massachusetts Institute of Technology, Cambridge, MA 02139, USA*
[b] *MIT Sea Grant College Program, Cambridge, MA 02139, USA*
[c] *Department of Mechanical and Materials Engineering, Queen's University, Kingston, Ontario K7M 3N9, Canada*
[d] *Ingenuity Labs, Queen's University, Kingston, Ontario K7M 3N9, Canada*

ARTICLE INFO

Article history:
Received 5 May 2021
Received in revised form 28 February 2022
Accepted 29 April 2022
Available online xxxx

Keywords:
VIV
Forced vibration
Hydrodynamic database
Optimization
Digital twin

ABSTRACT

We address the problem of obtaining accurate predictions of the vortex-induced vibrations (VIV) of flexible structures placed in cross-flow by reconstructing fluid force databases in parametric form. The forces are expressed in terms of hydrodynamic coefficients, which depend on several variables and parameters, including the structural properties and geometry, frequency and amplitude of vibration, and the flow conditions, so that a comprehensive database obtained with systematic experiments would require an intractably large number of tests. Therefore, we develop a method for determining optimal parametric hydrodynamic databases directly from a variety of free- and forced-vibration experiments on both rigid and flexible cylinders, by minimizing the error between the predicted responses using a software driven by the force database, and the measured data. We first describe the process of selecting an appropriate parametrization of the fluid forces as function of reduced frequency and non-dimensional amplitude of vibration, informed by Gaussian-Process-Regression-guided automated experiments. Several examples are selected to demonstrate the method's ability to acquire optimal hydrodynamic databases, including data sets highlighting the effect of Reynolds number and the addition of in-line motion to cross-flow rigid cylinder VIV. The proposed methodology is further demonstrated to be effective when used with the semi-empirical program VIVA for flexible cylinder VIV, yielding significant improvements in prediction accuracy compared to baseline results. It therefore serves as a potential solution for the development of a digital twin for marine risers, an in-situ, real-time riser response prediction and structural health monitoring system.

1. Introduction

Predicting vortex-induced vibrations (VIV) of a bluff body is a challenging problem of great theoretical interest that is also encountered in a broad range of engineering applications, such as marine risers and cables operating within ocean

---

[*] Corresponding author at: Department of Mechanical Engineering, Massachusetts Institute of Technology, Cambridge, MA 02139, USA.

E-mail addresses: shrudy@mit.edu (S. Rudy), dixia.fan@queensu.ca (D. Fan), jaguila@mit.edu (J.d.A. Ferrandis), sapsis@mit.edu (T.P. Sapsis), mistetri@mit.edu (M.S. Triantafyllou).

[1] Equal contributors.

https://doi.org/10.1016/j.jfluidstructs.2022.103607
0889-9746/

currents, and tall wind turbines. If the problem is not dealt with appropriately, VIV may result in fatigue damage and possible catastrophic failure with severe economic and environmental consequences. As a result, VIV is considered to be a canonical fluid–structure interaction (FSI) problem and has received significant research attention in the last four decades. Several publications (Williamson and Govardhan, 2004; Gabbai and Benaroya, 2005; Williamson and Govardhan, 2008; Bearman, 2011; Wang et al., 2020a) have reviewed the key concepts and principal mechanisms of the VIV response of a bluff body and the related vortical patterns in its wake.

The first studies of an elastically mounted rigid bluff body VIV, placed in uniform flow, addressed the cross-flow (CF) vibration only, omitting the in-line motions, which are typically smaller. Unsteady lift forces, caused by the shedding of alternating-sign vortices in the wake of the cylinder, result in sustained self-limiting vibrations with amplitudes up to one or two cylinder diameters (Williamson, 1996). Due to a strong coupling between the motion of the structure and the strength and location of the forming vortices, the fluid forces vary significantly as function of the structural and flow properties (Williamson, 1996; Xu et al., 2013; Chen et al., 2013). Therefore, systematic experiments have been conducted, where a rigid cylinder is forced to vibrate in the CF direction at prescribed frequencies and amplitudes (Sarpkaya, 1978) measuring the mean drag coefficient C_d, as well as the lift coefficient in-phase with velocity C_{lv} and the added mass coefficient in the CF direction C_{my} (Gopalkrishnan, 1993). Experimental results indicate that there is a region of positive C_{lv} located within a certain range of true reduced frequency $f_r = \frac{fD}{U}$ and non-dimensional CF amplitude $A^* = \frac{A_y}{D}$, where U is the prescribed fluid velocity, f is the prescribed motion frequency, A_y is the prescribed motion amplitude and D is the cylinder diameter.

However, subsequent studies with a cylinder that was allowed to move in both the in-line (IL) and the CF directions found considerable differences in the CF response (Aronsen, 2007; Dahl et al., 2010). For free vibrations of low mass ratio cylinders, the CF response can reach larger amplitudes (Jauvtis and Williamson, 2003), and within a wider synchronization frequency range (Dahl et al., 2010). Moreover, the phase θ between the IL and the CF motions was found to have a strong influence on the fluid forces (Le Garrec et al., 2016; Wu et al., 2017; Fan and Triantafyllou, 2017). The measured hydrodynamic coefficients are helpful in understanding the nature of the rigid cylinder free vibration, while they also provide a fluid force database to model the response of flexible risers within ocean currents. This approach is used, for example, in semi-empirical codes (Triantafyllou et al., 1999; Roveri and Vandiver, 2001; Larsen et al., 2001) that employ strip theory (Han et al., 2018; Fan et al., 2019b; Wang et al., 2020b) and the databases obtained from forced vibration experiments to model the sectional forces distributed along the riser length.

Due the significant computational resources required, high-fidelity numerical simulation of flexible cylinder VIV (Bourguet et al., 2011; Zhu et al., 2018) has focused on relatively low Reynolds numbers ($Re \sim O(10) - O(10^3)$) and small to medium aspect ratios ($L/D \sim O(10) - O(10^3)$), conditions which are different from those in full-scale riser operations ($Re \sim O(10^5)$ and $L/D \sim O(10^4)$). Therefore, the state-of-the-art riser VIV prediction tools widely adopted in the industry are still based on semi-empirical model predictions, whose results rely heavily on the accuracy of the hydrodynamic coefficients database constructed via rigid cylinder forced vibration experiments. Various studies have shown that these coefficients are sensitive to several parameters, including Reynolds number (Xu et al., 2013), riser configuration (Lin et al., 2020), turbulence in the oncoming stream, and surface roughness (Chang et al., 2011). Hence, a systematic development of a hydrodynamic database is virtually impossible. Furthermore, long-term effects such as equipment aging and bio-fouling inevitably alter the hydrodynamic coefficients throughout the lifetime of a riser, making prediction and monitoring even more challenging (Meng et al., 2020; Wu et al., 2020).

In this work we propose a methodology for determining parametric forms of hydrodynamic databases that can be trained with sparse sensors along the length of a riser. The structure of the proposed databases is informed by experiments performed on rigid cylinders using both free and forced vibrations and also tested on large scale experiments using flexible cylinders. We show that the proposed method yields accurate predictions for VIV amplitude and frequency both in the case of rigid and flexible cylinder experiments. Such a proposed method is promising for the construction of the future real-time digital twin system for structural health monitoring of marine production risers that will be deployed in the offshore system for decades, shown in Fig. 1.

The rest of the paper is organized as follows; In Section 2 we discuss the mathematical assumptions and models used in this work as well as the specifics of the proposed computational method. In Section 3 we test the method using experimental results from setups including crossflow only vibrations, crossflow and inline vibrations, and flexible cylinder vibrations. We conclude our work and discuss future directions in Section 4.

2. Materials and methods

2.1. Forced vibration VS. free vibration of cylinders

Databases for the hydrodynamic coefficient (C_d, C_{lv} and C_{my}), obtained by conducting rigid cylinder forced vibrations, can be used to predict the free vibrations of both rigid and flexible cylinders (Mukundan, 2008). A detailed experimental setup and procedure for rigid cylinder CF-only forced vibration is provided in Appendix E.

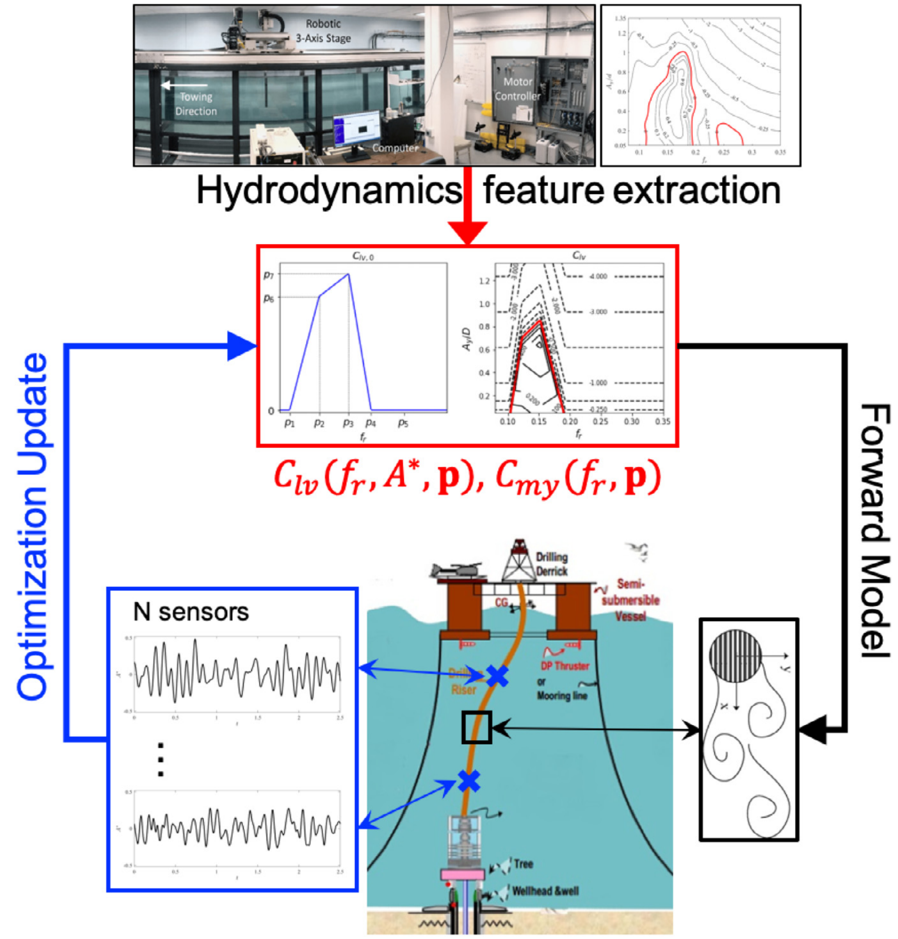

Fig. 1. Concept of the digital twin of a marine riser for real-time monitoring, using optimally learned hydrodynamic databases. First, parametric models of the hydrodynamic coefficients of bluff body VIV are derived from rigid cylinder forced- and free-vibration experiments. Based on the forward model that models the physics of the problem and real-time measurements from a few sensors located along the riser, the parameters are updated via optimization to construct an optimal hydrodynamic database and hence provide an improved structural response prediction.

2.1.1. Rigid cylinder VIV

For a rigid cylinder of mass m, diameter D and length L, mounted on a linear spring with constant k and a dashpot with damping constant b, placed within a uniform current of velocity U, the governing equation of motion is,

$$m\frac{d^2y}{dt^2} + b\frac{dy}{dt} + ky = F_l(t), \tag{1}$$

where $F_l(t)$ represents the oscillatory lift force acting from the fluid on the rigid cylinder. Assuming the system will achieve a steady state harmonic oscillation, $y(t) = Re\left\{Ae^{i\omega t}\right\}$, where A is the amplitude and ω the frequency, and $Re\{x\}$ denotes the real part of x, the lift force can be modeled as follows;

$$F_l(t) = Re\{[C_{my}\rho_f\forall + i(\frac{\rho_f U^2}{2})DLC_{lv}]e^{i\omega t}\}, \tag{2}$$

where ρ_f is the fluid density and $\forall = \frac{\pi}{4}D^2L$ is the cylinder displaced fluid volume. Substituting Eq. (2) into Eq. (1) and separating real and imaginary parts, we find the following set of equations in a non-dimensional form,

$$V_r(U_r) = U_r\sqrt{\frac{m^* + C_{my}}{m^* + 1}}, \tag{3}$$

$$A^*(U_r) = \frac{C_{lv}U_r^2}{4\pi^3(m^* + 1)\zeta}, \tag{4}$$

where $V_r = \frac{U}{fD}$ is the true reduced velocity, which is the inverse of the true reduced frequency $f_r = \frac{fD}{U}$, f is the response frequency, $U_r = \frac{U}{f_n D}$ is the reduced velocity, $f_n = \frac{1}{2\pi}\sqrt{\frac{k}{m+\rho_f \forall}}$ is the natural frequency of the system in the still water that is found assuming $C_{my} = 1.0$, $A^* = \frac{A_y}{D}$ is the non-dimensional CF amplitude of the response, $m^* = \frac{\rho_s}{\rho_f}$ is the mass ratio, ρ_s is the density of the mass m, and ζ is the damping ratio. The hydrodynamic coefficients C_{lv} and C_{my} depend on the input parameters V_r, A^* and Re and can be determined experimentally conducting forced vibrations on a rigid cylinder (Gopalkrishnan, 1993).

2.1.2. Flexible cylinder VIV

The free vibrations of a flexible cylinder within a sheared current can be predicted on the basis of rigid cylinder experimental data by using a strip theory approach (Fan et al., 2019b). For a vertical flexible cylinder, if we denote by z the vertical axis, and assume that the cylinder lies between $z = 0$ and $z = L$ with μ denoting the mass per unit length, c the structural damping per unit length, EI the bending stiffness, T the tension at the top, and $f_l(z, t)$ the time-varying fluid lift force per unit length in the CF direction at location z, the structural model for small amplitude vibrations can be written as,

$$\mu \frac{\partial^2 y}{\partial t^2} + c\frac{\partial y}{\partial t} - \frac{\partial}{\partial z}(T\frac{\partial y}{\partial z}) + \frac{\partial^2}{\partial z^2}(EI\frac{\partial^2 y}{\partial z^2}) = f_l(z, t). \tag{5}$$

As for a rigid cylinder, the riser monochromatic steady state oscillation can be expressed as $y(z, t) = Re\left\{Y(z)e^{i\omega t}\right\}$ where $Y(z)$ is a complex valued space-varying amplitude oscillating with frequency ω. The lift force $f_l(z, t)$ is modeled as,

$$f_l(z, t) = Re\{[C_{my}\rho_f \forall Y(z)\omega^2 + iC_{lv}\frac{\rho_f U^2}{2}D\frac{Y(z)}{|Y(z)|}]e^{i\omega t}\}. \tag{6}$$

Substitution of Eq. (6) into Eq. (5) produces a nonlinear eigenvalue problem given by,

$$[-\omega^2(m + C_{my}\forall) + i\omega b]Y - \frac{\partial}{\partial z}(T\frac{\partial Y}{\partial z}) + \frac{\partial^2}{\partial z^2}(EI\frac{\partial^2 Y}{\partial z^2}) = iC_{lv}\frac{\rho_f U^2}{2}D\frac{Y}{|Y|}, \tag{7}$$

where again, C_{my} and C_{lv} are functions of A^*, V_r and Re, which can be found from the hydrodynamic database obtained from rigid-cylinder, CF-only forced vibrations. Eq. (7) can be solved iteratively in semi-empirical codes such as VIVA (Triantafyllou et al., 1999).

2.2. Parametric hydrodynamic databases

Databases for the force coefficients C_m and C_{lv} include dependencies on a large number of independent variables including structural and flow parameters. This makes obtaining exhaustive databases extremely challenging due to the large amount of experimental data required. For example, experiments conducted at full scale Reynolds numbers require large scale experimental facilities and equipment at considerable costs. In addition, databases depend on time dependent parameters, such as surface roughness, which changes over the lifetime of a deployed riser due to marine growth and exposure to seawater. This makes the development of universal databases for ocean engineering applications from forced vibration experiments intractable.

This work seeks to address some of the challenges in constructing exhaustive databases by proposing a method for learning databases directly from field measurements. We construct parametric forms for both C_m and C_{lv} that capture salient and dynamically-relevant features present in a variety of experimental datasets from both free and forced vibration experiments. These parametric forms may then be used in tandem with the known governing equations for VIV and numerical solvers to obtain predictive models. Comparison with experimental results on a particular structure yields an optimization problem capable of learning optimal hydrodynamic databases even with free vibration experiments where no force measurements are taken. We present methods for learning databases from both rigid and flexible cylinder experiments.

The latter builds on work from (Mukundan, 2008), while taking into account data from recent experimental results. This approach has several benefits: First, free vibration experiments are easier to perform than forced vibration experiments and there are significantly more data available for free vibration cases under a variety of conditions, including data from deployed marine risers in the field. The learned databases are also structure specific, eliminating some of the independent variables affecting C_m and C_{lv} and may be easily adapted in time to account for structural changes due to environmental factors.

The parametric databases used in this work are informed by the experimental results obtain in Fan (2019). It is found that many of the known properties of C_{lv} and C_{my} may be captured in a simple piecewise linear model, although more complex models can be used as well. Based on experimental evidence, C_{my} is taken to be a function only of f_r, represented by three regimes of constant C_{my} separated by linear transitions, as shown in Fig. 2. Transitions between linear segments are smoothed by using a soft-plus function with a characteristic length scale that is treated as a learned parameter. C_{lv} is modeled as a piecewise linear function of the amplitude of oscillation, starting with a value $C_{lv,0}(f_r)$ at $A^* = 0$ that

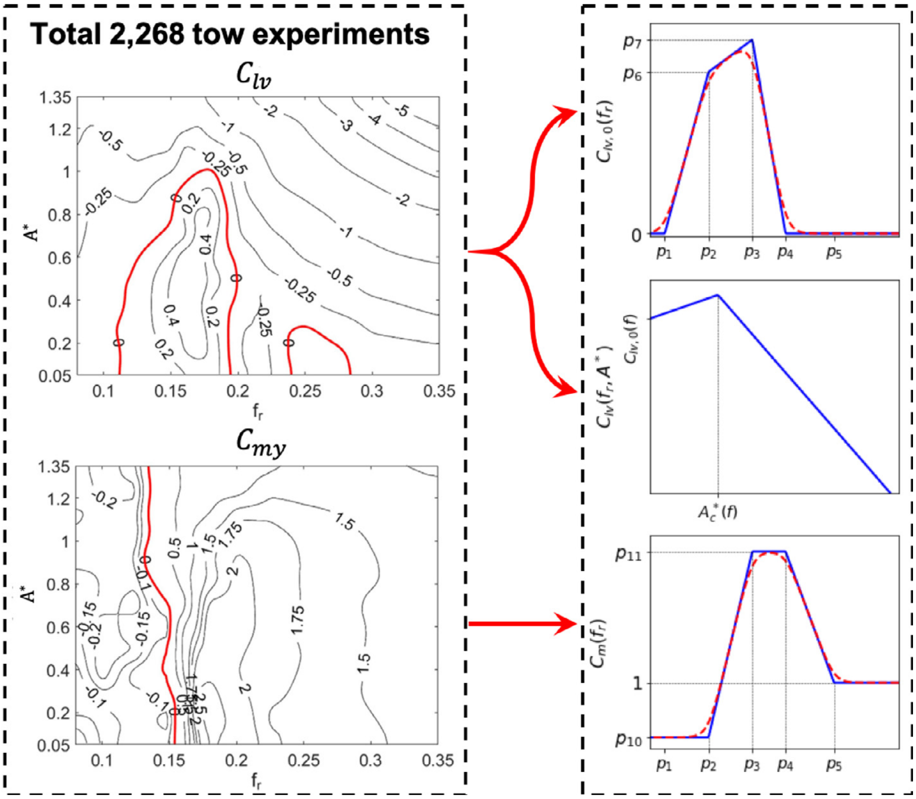

Fig. 2. A parametric representation of hydrodynamic coefficient database, constructed using a large number of rigid forced vibration experiments (left) (Fan et al., 2019a), and using simple piecewise linear models. The set of parameters defining the database are to be learned from field and experimental data (right).

is linearly increasing until A^* reaches a threshold value of A_c^*, above which C_{lv} linearly decreases as function of A^*. The values of $C_{lv,0}$ and A_c^* are each smoothed with piecewise linear functions of f_r, as shown in Fig. 2.

This process yields a model for hydrodynamic coefficients parametrized by fourteen variables; five parametric values of reduced frequency indicating boundaries between piecewise linear regimes are shared among C_{my}, $C_{lv,0}$, and A_c^*. Two additional parametric values are needed for each of C_{my}, $C_{lv,0}$, and A_c^* to completely define those functions; as well as two parameters expressing the slopes for computing C_{lv} as function of the amplitude. Each parameter is constrained to lie within a physically plausible region. It is noted that to accommodate the additional phenomena found in combined-CF-and-IL free vibration, another five variables are added to the parametrization model with a total of nineteen variables, which will be discussed in Section 3.2. The exact functional forms for each quantity as well as constraints on each parameter are given in Appendix B.

2.3. Predicting the structural response

Parameters for the hydrodynamic databases are found via numerical optimization by minimizing the difference between predicted responses made using the database and the observed structural response of a rigid or flexible cylinder. This requires a forward model leading from the assumed parameters $\mathbf{p}$, and the input variables to predictions, which will be different for rigid and flexible cylinders.

2.3.1. Database optimization for rigid cylinders

We begin by describing the forward model and objective function to be minimized for the case of a rigid cylinder. Consider an experimental dataset, where we have prescribed inputs, $\{(U_{r,j}, \zeta_j, m_j^*)\}_{j=1}^m$, and measured outputs $\{(A_j^*, f_{r,j})\}_{j=1}^m$. We assume that over the course of m experiments all other parameters, such as surface roughness and spring constant, have been maintained constant so that the same hydrodynamic database may be used. Assuming harmonic oscillations, we may use Eq. (4) and (3) to predict the structural responses $\{(\hat{A}_j^*, \hat{f}_{r,j})\}_{j=1}^m$, given the current value of the parameters $\mathbf{p}$. The optimal parametrization will be selected such that the difference between predictions and measured values is minimized.

We make predictions of the structural response by finding pairs $((\hat{A}^*, \hat{f}_r))$ such that the equations of motion result in minimal error. Inserting the predicted response into Eq. (4) and (3), and treating the difference between the left and right sides as errors, we find,

$$\begin{aligned} \text{frequency error} &= \left| \hat{f}_r^{-1} - U_r \sqrt{\frac{m^* + C_{my}(\hat{f}_r; \mathbf{p})}{m^* + 1}} \right| \\ \text{amplitude error} &= \left| \hat{A}^* - \frac{C_{lv}(\hat{f}_r, \hat{A}^*; \mathbf{p}) U_r^2}{4\pi^3 (m^* + 1)\zeta} \right|. \end{aligned} \tag{8}$$

The parameters in the representation of C_{my} and C_{lv} admit solutions that set the error terms to zero. It is in principle possible that there exist multiple values of reduced frequency that solve (8), but this has not been observed in the datasets used for this work. The expression for amplitude error always has a unique solution. We determine $\hat{f}_r$ and $\hat{A}^*$ and find the lowest and unique values yielding zero frequency and amplitude error, respectively. Details on determining $\hat{f}_r$ and $\hat{A}^*$ are given in Appendix C.

Summing over all observed experiments we obtain the rigid cylinder objective function that we seek to minimize;

$$J_r(\mathbf{p}) = \sum_{j=1}^{m} \frac{(f_{r,j} - \hat{f}_r(U_{r,j}, m_j^*; \mathbf{p}))^2}{\sigma_{f_r}^2} + \frac{(A_j^* - \hat{A}_j^*(U_{r,j}, m_j^*, \zeta_j, \mathbf{p}))^2}{\sigma_{A^*}^2}. \tag{9}$$

Here we have normalized each error term by the variance of the respective quantity in the dataset. We note that a similar objective function can be formed via the difference in the predicted reduced velocity rather than the reduced frequency. Doing so places more emphasis on those experiments with lower frequency. The current formulation was selected for two reasons: First, it was observed that the learned coefficients more closely resembled those available from forced vibration data; and second, it is often the case in applications that high frequency oscillations are of more interest, given that they will cause higher fatigue. However, differences between the two cases were observed to be small.

We summarize the optimization problem for the parametric hydrodynamics database as,

$$\hat{\mathbf{p}} = \underset{\mathbf{p}}{argmin}\, J_r(\mathbf{p}) + \mathcal{R}(\mathbf{p}), \tag{10}$$

where $\mathcal{R}(\mathbf{p})$ indicates regularization terms which penalize the width of the range of values of $\hat{f}_r$ where C_{lv} has positive values $(p_4 - p_1)$, the width of range of $\hat{f}_r$ where C_{my} is not constant $(p_5 - p_2)$ and the maximum value of A^* on the zero contour of C_{lv}. These terms were observed to yield more plausible results in some cases, but overall have a small effect.

2.3.2. Database optimization for flexible cylinders

For flexible cylinders, the assumption of harmonic motion yields the non-linear eigenvalue problem given by Eq. (7), which depends on the hydrodynamic databases for C_{lv} and C_{my}. We follow the approach first considered in Mukundan (2008) for learning optimal databases and solve Eq. (7) using the semi-empirical code VIVA (Triantafyllou et al., 1999). This yields a map from prescribed flow parameters to $\hat{A}^*(z; \mathbf{p}), \hat{f}_{peak}(\mathbf{z})$, which are predictions for multi-modal amplitude and peak frequency made by the semi-empirical code VIVA. The parameters are extracted from experimental data using the process outlined in Appendix F. We define the objective function as,

$$J(\mathbf{p}) = \sum_{(A^*(z), f_{peak}) \in \mathcal{D}} \left(\frac{1}{L} \int_0^L \left| A^*(z) - \hat{A}^*(z; \mathbf{p}) \right|^2 dz \right)^{\frac{1}{2}} + \lambda |f_{peak} - \hat{f}_{peak}(\mathbf{z})|, \tag{11}$$

where $A^*(z)$ and $f_{peak}(\mathbf{z})$ are experimentally measured values contained in a dataset $\mathcal{D}$ sampled at different flow velocities.

$$\hat{\mathbf{p}} = \underset{\mathbf{p}}{argmin}\, J_f(\mathbf{p}) + \mathcal{R}(\mathbf{p}), \tag{12}$$

In this work, we select a dataset obtained in the Norwegian Deepwater Programme (NDP) large-scale laboratory experiment (Braaten and Lie, 2004). The data were obtained from a 38 m uniform flexible riser placed within a uniform current with incoming velocity ranging from 0.3 m/s to 2.4 m/s. The details of the NDP experiment and the corresponding dataset are presented in Appendix F.

2.4. Optimization routine

The optimization problems described in Eqs. (10) and (12) are computationally stiff and non-smooth due to the internal solver. We found that gradient based methods often fail to find a descent direction using finite difference approximations of the gradient.

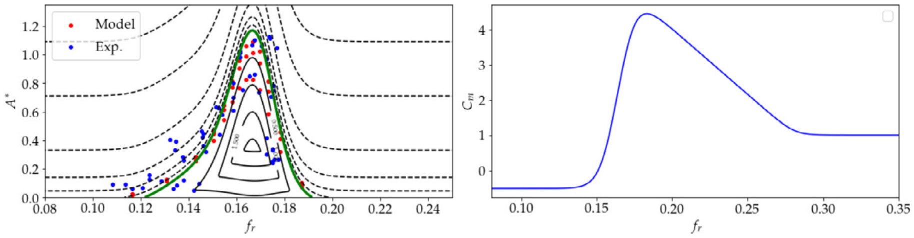

Fig. 3. The constructed C_{lv} (left) and C_{my} (right) based on the optimal parameters learned from the free vibration experiment (Smogeli et al., 2003). The blue and red dots in the C_{lv} contour indicate experimental and predicted values of A^* and f_r. The maximum value of C_{lv} is 2.144 occurring at $(f_r, A^*) = (0.167, 0.35)$. The maximum value of A^* on the zero contour of C_{lv} is $A^*_{max} = 1.189$ when $f_r = 0.167$.

Previous approaches to the flexible cylinder problem have used the Nelder–Mead algorithm (Gao and Han, 2012) or simulated annealing (Kirkpatrick et al., 1983) to optimize a cost function similar to Eq. (12) (Mukundan, 2008). For the problems considered in this work we found coordinate descent (Wright, 2015) to exhibit superior performance on both Eqs. (10) and (12). Coordinate descent algorithms iterate through each dimension of $\mathbf{p}$ and solve the one-dimensional problem given by,

$$p_i = \underset{y}{argmin}\, J(p_1, \ldots, p_{i-1}, y, p_{i+1}, \ldots) + \mathcal{R}(p_1, \ldots, p_{i-1}, y, p_{i+1}, \ldots). \tag{13}$$

Eq. (13) is generally solved via line search, or closed form expressions when available. The loss functions considered in this work exhibit irregular behavior including plateaus, which make determining a descent direction and step size for line search methods challenging. We found that more rapid convergence could be found via evaluating the cost function at random perturbations of the current estimate along a fixed direction and selecting the best value. Specifically, we iteratively set $\mathbf{p} = \mathbf{p} + \delta_i \mathbf{v}_i$ where,

$$\delta_i = \underset{\delta \in \Delta}{arg\,min}\, J(\mathbf{p} + \delta \mathbf{v}_i) + \mathcal{R}(\mathbf{p} + \delta \mathbf{v}_i), \tag{14}$$

and $\Delta = \{0, \delta_1, \ldots, \delta_{n_{samp}}\}$ includes 0 and n_{samp} samples from some distribution p_δ, and $\mathbf{v}_i$ is a search direction. This bears a strong resemblance to other random search methods and simulated annealing in the low temperature limit. Details of the method including choices for p_δ, n_{samp}, and initialization may be found in Appendix D. Eqs. (10) and (12) are also non-convex and benefit from multiple trials of the optimization scheme as computational resources allow.

3. Results and discussion

In this section we demonstrate the application of the proposed methodology to several datasets. We start with 2 experimental datasets for crossflow only VIV in Section 3.1. In one dataset, a special experimental design allows us to compare learned hydrodynamic coefficients to those obtained via feedback control. In Section 3.2 we learn hydrodynamic databases from experimental results with a setup allowing for combined cross-flow and in-line motion. Finally, Section 3.3 shows the application of the proposed method to large scale flexible cylinder experiments. Results for the flexible cylinder are compared to the nominal database used by the semi-empirical solver VIVA (Zheng et al., 2011), which has been validated on a number of experimental datasets. The framework developed in the previous section for optimizing VIV databases will be referred to as VIVopt.

3.1. CF-only rigid cylinder free vibration

In this subsection, we present two cases of learning hydrodynamic databases from a small set of cross-flow only free vibration experiments. The detailed hydrodynamic coefficient functional representation is presented in Appendix A and is validated via a comparison between the GPR and VIVopt result of the forced vibration experiment of different *Re* in Appendix E.

3.1.1. Validation case of fixed $Re = 20{,}000$

Our first example uses data from (Smogeli et al., 2003). Using a force feedback laboratory apparatus (Hover et al., 1997), Smogeli et al. (2003) studied CF-only free vibration of a rigid cylinder over a large range of U_r with fixed $Re = 20{,}000$. Since this experimental setup allows for measurements of forcing in free vibrations, we consider it an excellent validation case for the proposed method. The structural properties were selected to have mass ratio of $m^* = 4$ and various damping ratios of $\zeta = 0.01$, $\zeta = 0.02$, and $\zeta = 0.05$. We find optimal parameters for the parametric hydrodynamic database using measured f_r and A^* across three values of ζ and all U_r cases. The resulting databases for C_{lv} and C_{my} are plotted in Fig. 3. The result shows that the learned C_{lv} contours are similar to previously obtained CF-Only forced vibration results (Gopalkrishnan, 1993) at a different $Re = 10{,}000$, exhibiting a narrow region of positive C_{lv} around $f_r = 0.16$

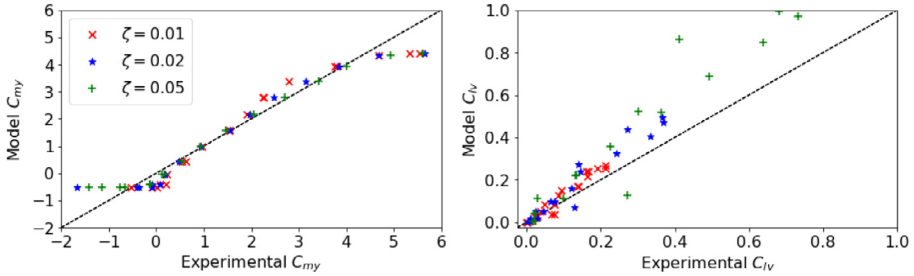

Fig. 4. The correlation between the experimentally measured (Smogeli et al., 2003) and the predicted C_{my}(left) and C_{lv} (right). The dashed line shows where experimental and prediction results are equal.

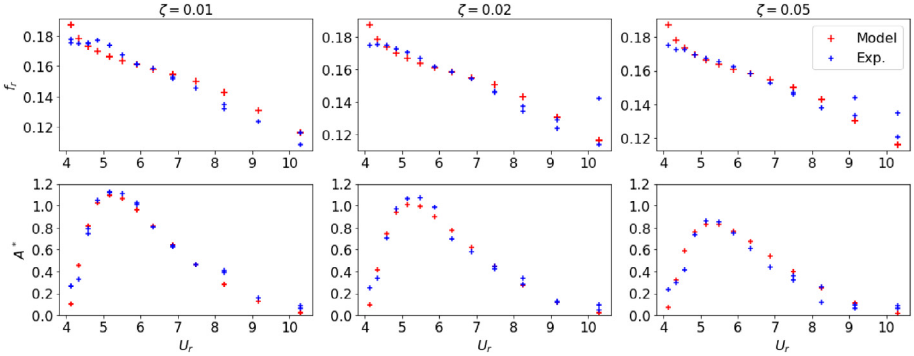

Fig. 5. Comparison between experiment (blue crosses) (Smogeli et al., 2003) and prediction (red crosses) for frequency (top row) and displacement (bottom row), for $\zeta = 0.01$ (first column), $\zeta = 0.02$ (second column) and $\zeta = 0.05$ (third column).

with maximum A^* of zero contour line reach $A^* = 1.2$. Meanwhile, the learned C_{my} is shown to have a drastic change from a small negative value to a large positive value at $f_r = 0.15$, similar to the findings in Gopalkrishnan (1993) and Carberry et al. (2005).

In Smogeli et al.'s experiment, both the structural and fluid responses were measured and recorded; hence the corresponding hydrodynamic coefficients can be obtained directly and we can compare the experimentally measured hydrodynamic coefficients with our learned optimal C_{lv} and C_{my} database. We plot the results in Fig. 4. The two sets of data show good linear correlation, indicating that the optimized hydrodynamic database learned from the free vibration data, matches well with the experimentally measured vortex-induced forces.

It is apparent from Fig. 4 (right) that the predicted C_{lv} is slightly larger than the experimentally measured C_{lv}. This may reflect approximations made by the proposed method and could also be a result of the experimental error due to the force-feedback setup (Hover et al., 1997). The maximum value of C_{lv} for the learned database is 2.144. This value is substantially higher than measured and theoretically plausible values. However, the maximum predicted C_{lv} at a location where data was collected is 0.996 when $U_r = 4.85$ and $(f_r, A^*) = (0.170, 0.756)$. Thus, clipping the predicted C_{lv} at 0.996 would yield a more physically plausible maximum value of C_{lv} while not affecting predictions.

A comparison between the experimental and model predicted response is shown in Fig. 5. As for the hydrodynamic coefficients, we observe good agreement between predictions and experimental data. As expected, for increase ζ, the maximum A^* decreases.

3.1.2. Reynolds number effect on maximum A^*

For CF-Only vibration, the hydrodynamic coefficients are not only affected by A^* and f_r, but are also strongly influenced by the Reynolds number Re (Fan et al., 2019a). Various experiments on rigid cylinder CF-only free vibration in moderate Re numbers (Govardhan and Williamson, 2006) reveal that the maximum A^* in an oscillating cylinder can increase significantly as Re increases toward the critical Reynolds number. In this subsection, we extract the hydrodynamic coefficients of rigid cylinder CF-only vibration at high Re from Lee et al.'s experiments (Lee and Bernitsas, 2011). We also provide the maximum A^* of a CF-only vibrating rigid cylinder with zero damping for several Re, using hydrodynamic databases constructed from different sources over a wide range of Re. We compare these predictions with existing experimental results.

Lee and Bernitsas (2011) conducted experiments on a rigid cylinder supported with springs of different stiffness and controlled damping ratios. They achieved a large range of U_r corresponding to various Re by changing the incoming flow speed. In the current work, the optimal parameters for hydrodynamic coefficient databases are hence learned from the

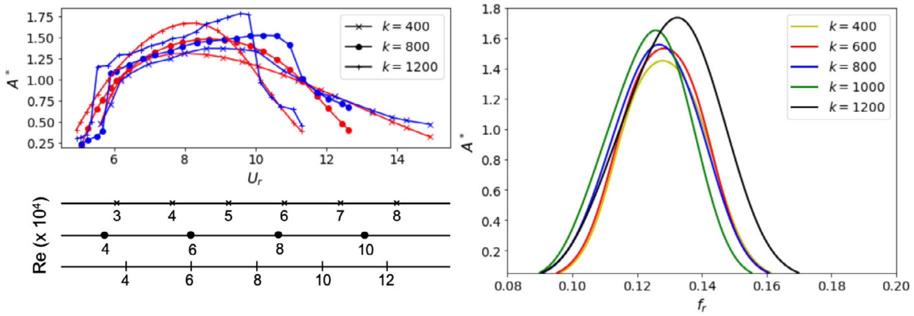

Fig. 6. Left: Comparison of displacement response between experiment (blue) and prediction (red). The corresponding *Re* is also provided. Right: The zero contour line versus f_r and A^*, learned from Lee's experiments at different values of the spring stiffness, corresponding to different *Re*. In the bottom of the left figure, the different scales represent the *Re* for the three sets of the experiments, corresponding to different values of the stiffness.

Table 1
Key features of learned databases for data from (Lee and Bernitsas, 2011). Each row corresponds to a given spring constant and includes the maximum value of C_{lv} for that database, along with its corresponding (A^*, f_r) coordinates, as well as the maximum A^* on the zero contour of C_{lv} and corresponding f_r.

k	$C_{lv,max}$	$A^*(C_{lv,max})$	$f_r(C_{lv,max})$	$A^*_{max}\|_{C_{lv}=0}$	$f_r(A^*_{max}\|_{C_{lv}=0})$
400	0.789	0.130	0.922	1.452	0.128
600	0.894	0.129	0.956	1.535	0.128
800	0.922	0.127	1.038	1.559	0.127
1000	1.048	0.126	1.175	1.653	0.126
1200	1.190	0.133	1.196	1.737	0.133

Table 2
Symbols for source of the data in Fig. 7.

Source	m^*	ξ	Symbol
Govardhan and Williamson (2006)	10	0	o
Raghavan and Bernitsas (2011)	1.8–3.4	0.08–0.14	∗
Ding et al. (2004)	1	–	■
Lucor et al. (2004)	2	0	♦
Lie et al. (2013)	2.1	0.01–0.02	×
Vikestad (1998)	1.277	0.147	△
Smogeli et al. (2003)	1.8–3.5	0.01	+
Hover et al. (1998)	4	0.013	★
Klamo et al. (2005)	7.1	0.011	◀
Forced vibration prediction	–	–	●

structural response for various cases, each having distinct spring stiffness. A comparison of the experimental and predicted A^*, as well as the $C_{lv} = 0$ contour for several spring constants are shown in Fig. 6. Fig. 6 (left) compares the displacement obtained with the different stiffness values. The horizontal axis corresponds to a different *Re* range for each *k*, which is marked below the axis. Experimental values are shown in blue and the prediction in red. It is shown that the learned optimal hydrodynamic database can predict well the displacement of the free vibration response provided by Lee et al. Furthermore, the $C_{lv} = 0$ contour line of the learned hydrodynamic database for different stiffness cases, corresponding to different *Re* ranges, are plotted in Fig. 6(b) versus A^* and f_r. With an increase of the stiffness, and thus an increase of *Re* for the same U_r, we observe an increase of the maximum A^* obtained by the $C_{lv} = 0$ contour line. Critical features of each of the learned databases shown in Fig. 6 are summarized in Table 1.

To show the *Re* effect on A^* for CF-only vibrations in uniform inflow, we summarize several experimental data and current predictions, over a large range of *Re*, in Fig. 7. The source of the data for Fig. 7 are listed in Table 2. Experimental results from (Klamo et al., 2005; Govardhan and Williamson, 2006; Martins and Avila, 2019) are taken in the sub-critical *Re* region before the onset of the fully turbulent shear layer (TrSL3) (Zdravkovich, 1997b). As *Re* increases, the maximum A^* reaches a peal amplitude of over 2 before dropping sharply to around 0.8 in the super-critical regime (Raghavan and Bernitsas, 2011). The predicted A^* of a zero-damped cylinder vibration based on the $C_{lv} = 0$ from the learned hydrodynamic coefficient database has also been plotted in green dots in Fig. 7, for comparison. The results show that the forced vibration experiments capture well the *Re* effect on the maximum CF amplitude of the free vibration.

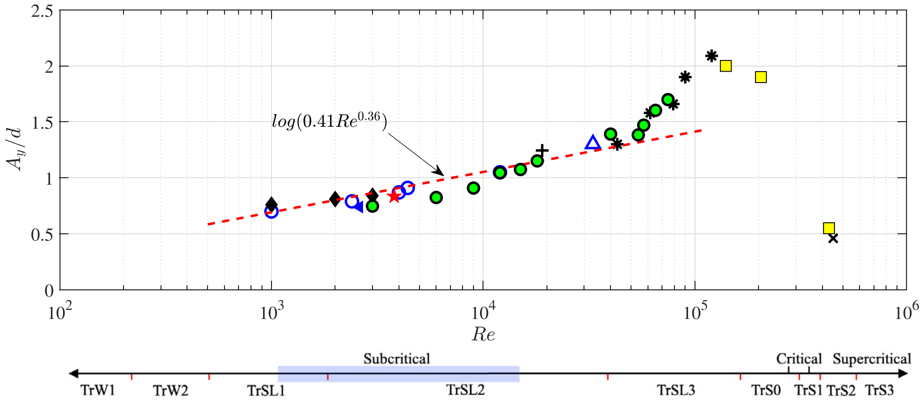

Fig. 7. The maximum CF amplitude A^* versus Re for CF-only vibration. The sources of the data are listed in Table 2. The red dashed line is the predicted motion for a zero-damped CF-only vibrating cylinder (Govardhan and Williamson, 2006). The Re range scale also indicates the flow patterns observed in a stationary rigid cylinder (Zdravkovich, 1997a; Raghavan and Bernitsas, 2011): "TrW1": transition to laminar vortices in the wake; "TrW2": transition to irregular vortices in the wake; "TrSL1": wave development in the free shear layer; "TrSL2": vortices form in the free shear layer; "TrSL3": fully turbulent shear layer; "TrS0": onset of transition at the separation point; "TrS1": single separation bubble; "TrS2": two separation bubbles; "TrS3": super-critical regime - fragmented separation bubbles. The green dots denote the predicted CF amplitude of a cylinder undergoing CF-only free vibration. The source of the data is listed in Table 2.

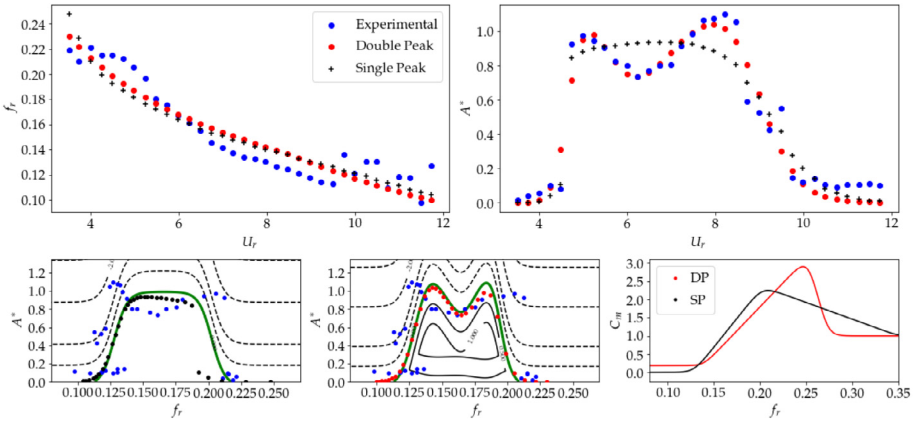

Fig. 8. Comparison between experimental data and predictions of A^* in combined-CF-and-IL rigid cylinder free vibration (Dahl et al., 2010). The first row shows the frequency (left) and the amplitude (right) response from experiment (blue dot), prediction using CF-only parametrization (black cross), and prediction using combined-CF-and-IL parametrization (red dot). The comparison of the learned hydrodynamic database using CF-only and combined-CF-and-IL parametrization is shown in (c) for CF-only parametrization and (d) for combined-CF-and-IL parametrization of C_{lv}, and (e) for C_{my}.

3.2. CF-and-IL-combined rigid cylinder free vibration

Experimental results have shown that in cylinders undergoing in-line (IL) as well as cross-flow motion, the combination qualitatively and quantitatively changes the relation between the CF A^* and U_r. In particular, it is observed experimentally that when the IL natural frequency is close to twice the CF natural frequency the CF displacement response has two distinct peaks as function of U_r (Dahl et al., 2010). To capture this phenomenon, we modified the hydrodynamic coefficient parametrization to accommodate such a qualitative change. Specifically, we allow $C_{lv,0}$ and A_c^* to have multiple peaks. Such a model ignores the coupling effect between the IL and the CF vibration, in particular, the phase angle between two directions, which is subjected to the future research. A more detailed explanation of the parametrization is given in Appendix B. We test both single and double peak parametrizations using the data from the IL-CF-combined free vibration experiment by Dahl et al. (2010). The resulting responses and learned hydrodynamic databases are shown in Fig. 8. The difference between the two parametrizations can be seen clearly in Fig. 8(b) together with a comparison with the experimental results. The double peak parametrization accurately captures the double peak of the displacement response in the CF direction, while the single peak parametrization fails to do so. The same difference is reflected from the learned C_{lv} contour using the previous parametrization of Fig. 8(c) and the new parametrization of Fig. 8(d). Meanwhile, it is found that the predicted frequency ratios using either parametrization match well the experimental result, as shown in

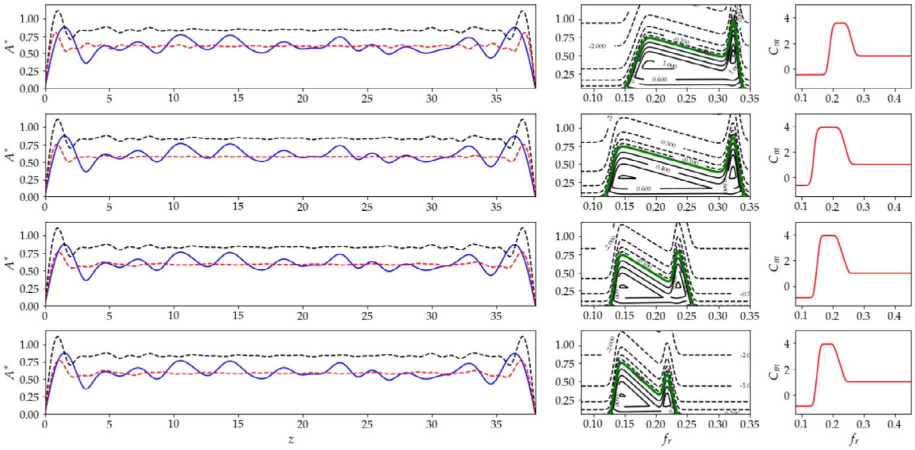

Fig. 9. Evolution of VIVA predictions for the NDP experiments at $U = 2.0$ m/s, as parameters are varied; for iteration 0 (first row), iteration 1 (second row), iteration 5 (third row), iteration 10 (fourth row). In the left column, the solid blue line shows the experimental results; the black dashed line shows the nominal VIVA prediction, and the red dashed line shows the VIVA prediction with corresponding learned hydrodynamic databases that are shown in the middle column for C_{lv} and right column for C_{my}. Additionally, the measured frequency response is 10.23 Hz in the experiment, the nominal VIVA prediction is 12.54 Hz, and with the improved hydrodynamic database, the predicted frequency response evolves as 13.91 Hz (iteration 0), 10.84 (iteration 1), 10.70 (iteration 5) and 10.70 (iteration 10).

Fig. 8(a). Using the two peak model, we find that the maximum value of C_{lv} is 1.47 when $(f_r, A^*) = (0.184, 0.446)$ and the maximum value of A^* on the zero contour of C_{lv} is $A^*_{max} = 1.108$ when $f_r = 0.184$.

3.3. Free vibration of flexible cylinders in uniform flow

We solve Eq. (11) using data from the NDP experiment (Braaten and Lie, 2004) on a 38 m uniform flexible riser placed in uniform current with incoming velocities ranging from 0.3 m/s to 2.4 m/s. To demonstrate the learning process, we plot in Fig. 9 the evolution of the VIVA prediction with the hydrodynamic database over the initial, first, fifth and tenth iterations, for the $U = 2.0$ m/s case (NDP experiment no. 2182). The left column shows the comparison between the prediction and the experiment. We can see that as iterations progress, the difference between the experimental results and VIVA predictions improve. Furthermore, the last row of the displacement plot shows that with a learned optimal hydrodynamic database (solid blue line), VIVA can provide a better prediction than that using the standard hydrodynamic database (red dashed line), as compared to the experimental results (solid black line). The middle column in Fig. 9 plots the corresponding C_{lv} of the learned parameters $\mathbf{p}$, and it can be shown that the hydrodynamic database C_{lv} does not vary much for larger iterations, representing a convergence of the learning process. Additionally, the measured frequency response is 10.23 Hz in the experiment, the nominal VIVA prediction is 12.54 Hz, and with the improved hydrodynamic database, the predicted frequency response evolves as 13.91 Hz (the initial guess), 10.84 (the first iteration), 10.70 (the fifth iteration) and 10.70 (the tenth iteration). We can conclude that with the converged optimal hydrodynamic database; VIVA can provide a better prediction on the frequency response.

From Fig. 9 it is apparent that the mean response amplitude is largely unchanged over the course of the optimization routines progress. Indeed, changes are largely restricted to the oscillating regions near each boundary. This indicates that the initialization of the optimization routine, discussed in Appendix D, yields parameters with low amplitude error and that fine tuning is dominated by improvements in frequency. This should not, however, be taken to indicate that the database does not affect amplitude, as is evidenced by the large difference in predicted amplitude between the nominal and optimized databases.

The displacement response A^* along the flexible cylinder span, for all velocities, is shown in Fig. 10 for the experimental results (left), VIVA predictions using the nominal hydrodynamic database (middle: referred to as the nominal VIVA prediction), and using the optimized hydrodynamic database (right: referred to as the optimized VIVA prediction). With increasing velocity, the vortex shedding frequency increases, and we observe an increasing amplitude of the vibration mode for all three results. However, large amplitude difference can be seen between the nominal VIVA prediction and the experimental result, while the optimized VIVA prediction shows a better match to the experimental response.

It is noteworthy that the $C_{lv} = 0$ contour line in the learned database for the NDP data achieves a maximum A^* that is lower than that of the database for rigid cylinder CF-and-IL vibrations despite higher Reynolds number. Since both tests were performed at sub-critical Reynolds number, this result conflicts with trends observed in Fig. 7. However, the result agrees in each case with experimental values of A^*. This can be taken as evidence for either an effect of flexibility of the cylinder on A^*, or on some unresolved source of experimental or model error. Another notable difference is that while the region where $C_{lv} > 0$ has similar bounds on the f_r axis, the shape with regards to A^* is different. There are several plausible

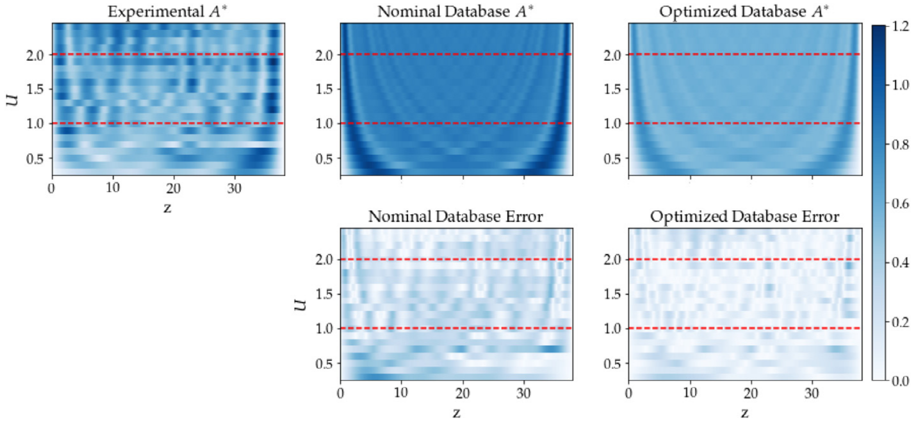

Fig. 10. (Color online) Experimental (left), VIVA prediction nominal (middle) and optimized (right) results of the displacement response in the CF direction as function of z/d and incoming velocity $U(m/s)$ for the 38 m flexible cylinder in uniform flow in the NDP experiments. The dashed lines indicate the selected cases of $U = 1.0$ m/s and $U = 2.0$ m/s shown in Fig. 11. Absolute error of predictions from nominal and optimized databases are shown on second row.

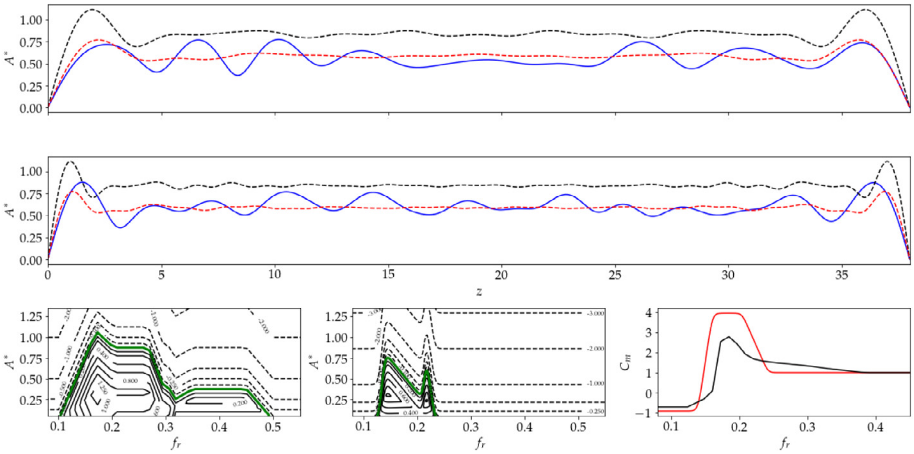

Fig. 11. Comparison of the response prediction and fluid force database between the nominal and optimized VIVA. The top two rows plot the comparison of the displacement response A^* along the flexible cylinder span for the experimental results (sold blue line), nominal VIVA prediction (black dashed line), and optimized VIVA prediction (red dashed line), for the case $U = 1.0$ m/s (first row), and $U = 2.0$ m/s (second row). The comparison of C_{lv} database is plotted in the first and second column of the third row used in the nominal (left column) and optimized (middle column) VIVA. The comparison of C_{my} used in the nominal and optimized VIVA is plotted in the right column of the third row.

explanations for this difference including Reynolds number effects and errors in parameterizations of or assumptions used in the forward models. Any such errors will be accounted for via an adjusted optimal database. Therefore, databases learned using the VIVopt framework should be considered specific to the experimental or field apparatus they are trained on.

Fig. 11 shows the experimental results, as well as nominal and optimized database predictions for two of the velocities from Fig. 10, $U = 1.0$ m/s and $U = 2.0$ m/s. It can be clearly seen that the nominal VIVA prediction (black dashed line) over-predicts the experimental result significantly, roughly doubling the experimental magnitude. In contrast, the optimized VIVA prediction (red dashed line) accurately captures the magnitude of A^* along the span of the cylinder. Additionally, we plot the comparison of the hydrodynamic coefficients of C_{lv} and C_{my} used in the nominal and optimized VIVA predictions. For C_{lv}, compared to the nominal VIVA prediction, the optimized hydrodynamic database has a smaller positive area from $f_r = 0.15$ to $f_r = 0.28$. For C_{my}, it is shown that in the nominal VIVA prediction, C_{my} has a much sharper transition from the negative to the positive value at a smaller $f_r = 0.20$. The maximum value of C_{lv} in the learned database is 1.037 when $(f_r, A^*) = (0.145, 0.305)$ and the maximum value of A^* on the zero contour of C_{lv} is $A^*_{max} = 0.753$ when $f_r = 0.145$.

We summarize the improvements made to the nominal database by solving Eq. (11) in Fig. 12. We plot the peak response frequency f_{peak} and the mean disturbance $\overline{A^*} = \frac{1}{L}\int_0^L A^* dz$ for all velocity cases of the NDP experiment. The result

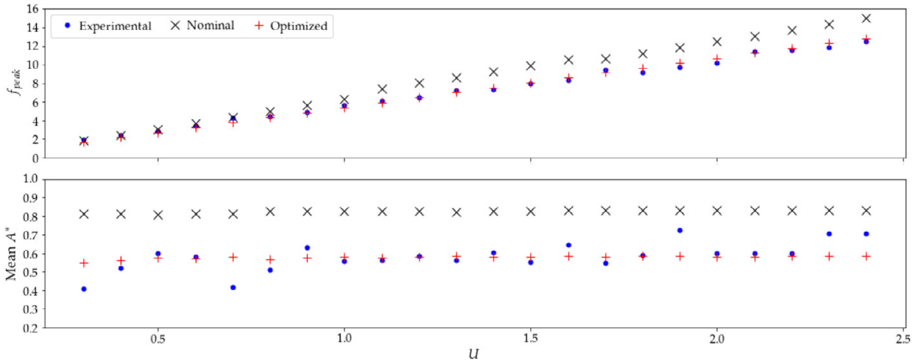

Fig. 12. Comparison of the peak response frequency f_{peak} (top row) and the spatially average $\overline{A^*}$ (bottom row) for all velocities, in the experimental results, nominal VIVA predictions and optimized VIVA predictions.

shows that the optimized hydrodynamic database exhibits greater accuracy in both frequency and amplitude prediction compared to the nominal database and that improvements are universal across all velocities.

4. Conclusions

This work has developed a robust method for constructing optimal hydrodynamic databases for vortex induced vibrations of rigid and flexible cylinders directly from free vibration experiments, rather than using forced vibration experiments. The process starts by constructing a low-dimensional parametric representation of the hydrodynamic databases that captures the major characteristic features observed in a large variety of previous rigid cylinder experiments. Therefore, we exploit known VIV physics to construct a forward model from the parametric databases to an estimated response, which we are able to compare with experimental data. An optimization routine is then applied to determine a suitable set of parameters that reflects the observed dynamics for the experimental design. The method yields accurate predictions of the VIV responses to given conditions and is shown to be effective across a variety of Reynolds numbers, scales, and structural properties .

The method is evaluated using a large variety of experimental datasets, ranging from CF-only rigid cylinder free vibration to large-scale flexible cylinder towing experiments. Beginning with rigid vibration experiments, the method has been successfully used to capture various rigid cylinder free vibration phenomena, such as the increase of the maximum amplitude response with increasing *Re* and the double amplitude response peak for the combined-IL-and-CF rigid cylinder free vibration. The proposed method seamlessly generalizes to flexible cylinder VIVs via integration with the semi-empirical VIV prediction software, VIVA. By applying the proposed parametrization and optimization framework, we are able to considerably reduce the error between semi-empirical predictions and experimentally observed values of frequency and amplitude compared to the nominal database used by VIVA. The VIVopt method has also been applied datasets including flexible cylinders in a shear flow (Rudy et al., 2021), yielding improvements over nominal database in amplitude and frequency prediction on par with those observed in this manuscript. Future work will consider cases such as steel catenary riser configurations or cylinders with variable width. The present work demonstrates wide applicability to both rigid and flexible cylinder VIV with both CF-only and CF and IL vibrations.

Databases constructed in this manuscript have been trained on sets of experimental data covering a small fraction of the domain in (f_r, A^*)-space on which we quantify hydrodynamic coefficients. Therefore, visualization of databases on the larger domain requires extrapolating. We have informed the parametric forms of databases by what has been observed in forced vibrations tests and what captures salient features in historical databases. It is therefore reasonable to assume that the learned databases correctly approximate the true hydrodynamics within a neighborhood of observed data. However, for frequencies far from those observed in training data, databases should be treated as having a great amount of uncertainty and predictions made in such domains flagged as uncertain. Quantifying such uncertainty would be a fruitful direction for future research.

In summary, the proposed method has shown great promise for constructing complex VIV hydrodynamic databases and improving prediction of rigid and flexible cylinder free vibrations using only a small amount of data. However, it is important to point out that to achieve a universal database can be difficult (Wu et al., 2020), due to the multiple factors including co-existing multi-frequency components (Fan et al., 2019a), non-stationary and chaotic vibration patterns owing to time and space-varying excitation regions (Modarres-Sadeghi et al., 2011), and multiple cylinder interaction (Lin et al., 2020). Therefore, more complex hydrodynamic database modeling is required with advanced understanding of the VIV phenomena.

Furthermore, we highlight that the timescale over which new models may be trained from experimental data is significantly shorter than the timescale on which structural properties for field deployed structures changes. The proposed method is thus promising as a tool for constructing future long-term, in-situ and real-time riser structural response prediction and health monitoring system, a digital twin for marine riser, shown in Fig. 1.

Table A.3
Nomenclature.

Symbol	Description	Symbol	Description
A^*	Amplitude ratio A_y/D	m	Mass
A^*_c	Critical A^*	n_{samp}	Number of samples
A_y	Amplitude in y-direction	$\mathbf{p}$	Database parameter vector
b	Damping constant	p_δ	Sampling dist for δ_i
c	Struct. damp. per unit length	$\mathbf{v}$	Search direction
C_d	Drag coefficient	$\mathbf{q}$	Unconstrained parameter vector
$C_{lv,0}$	Lift force at zero amplitude	Re	Reynolds number
C_{lv}	Lift coeff. in phase with velocity	U	Fluid velocity
C_{my}	Added mass coefficient	U_r	Nominal reduced velocity
D	Cylinder diameter	V_r	True reduced velocity
EI	Bending stiffness	z	Length along cylinder
f	Frequency	δ_i	Random perturbation
f_l	Lift force per unit length	λ	Frequency weight in loss function
F_l	Lift force	μ	Mass per unit length
f_n	Natural frequency	ρ_s	Structure density
f_{peak}	Peak frequency	ρ_f	Fluid density
f_r	Reduced frequency	θ	Phase between CF & IL motion
k	Spring constant	ζ	Damping ratio
L	Cylinder length	$\forall$	Cylinder displacement
m^*	Mass ratio		

CRediT authorship contribution statement

Samuel Rudy: Methodology, Software, Formal analysis, Writing – original draft, Funding acquisition. **Dixia Fan:** Methodology, Data curation, Formal analysis, Writing – original draft. **Jose del Aguila Ferrandis:** Methodology, Software, Data curation, Writing – original draft. **Themistoklis P. Sapsis:** Supervision, Writing – review & editing. **Michael S. Triantafyllou:** Conceptualization, Project administration, Supervision, Writing – review & editing, Funding acquisition.

Declaration of competing interest

The authors declare that they have no known competing financial interests or personal relationships that could have appeared to influence the work reported in this paper.

Acknowledgments

The authors acknowledge support from the MIT Digital Twin of Marine Risers Consortium, USA (ExxonMobil, Subsea 7, Shell, Petrobras, ABS, SAIPEM), and by Chevron, USA and BP. SR and TPS would also like to acknowledge support from the National Science Foundation, USA under AwardNo. 1902972.

Appendix A. Nomenclature

Table A.3 includes a nomenclature of symbols found in the main body of the paper. In addition, we use the following acronyms: VIV: vortex induced vibrations
FSI: fluid structure interaction
CF: cross-flow
IL: in-line
GPR: Gaussian process regression
NDP: Norwegian Deepwater Program

Appendix B. Description of parametric forms for C_{lv} and C_{my}

In this section we describe the two parametrizations used for representing hydrodynamic databases. The single peak parametrization consists or fourteen parameters and the double peak parametrization has nineteen parameters. Descriptions of each parameter are shown in B.4. The functional forms considered in this work are inspired by past works using piecewise linear databases (Mukundan, 2008), but have been adjusted to allow for smoothing of the corners between linear components. To do this, we use the soft-plus function, given by,

$$s_w(x) = w\ \log(1 + exp(x/w)). \tag{B.1}$$

The parameter w is a length-scale over which the function transitions from near 0, for $x < 0$ to nearly x, for $x > 0$. The soft-plus function converges uniformly to the rectified linear unit as $w \to 0$, thus making the parameterizations used in this work a generalization of the piecewise linear case.

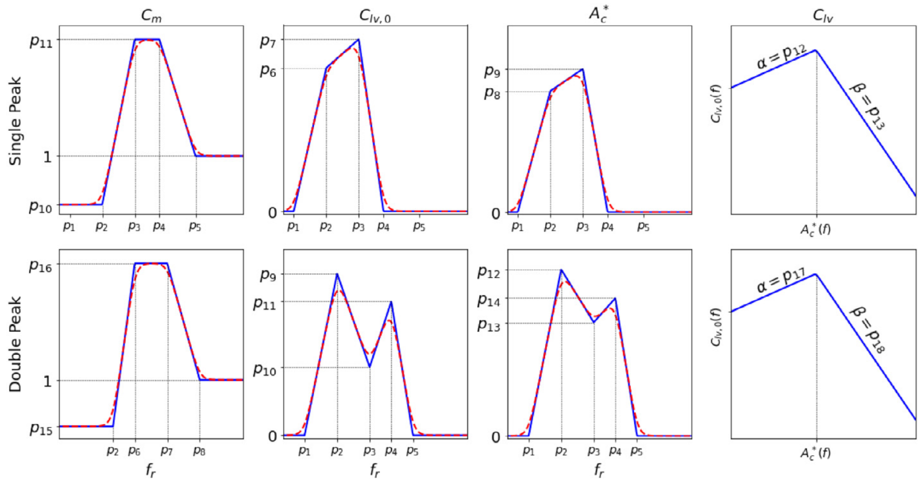

Fig. B.13. Single and double peak parametrizations used for C_{lv} and C_{my}. Blue curve shows piecewise linear parametrization realized when $p_{14} = 0$ (single peak) or $p_{19} = 0$ (double peak). Red dashed line is smoothed version from $p_{14/19} = 0.003$.

Table B.4
Description of parameters for single peak hydrodynamic database.

$p_1 - p_5$	Reduced frequencies used for C_m, $C_{lv,0}$, and A_c^*.
p_6, p_7	Parameters for values of $C_{lv,0}$ at p_2, p_3.
p_8, p_9	Parameters for values of A_c^* at p_2, p_3.
p_{10}, p_{11}	Values of constant sections of C_m curve.
p_{12}	Increasing slope of C_{lv} w.r.t. A^* for $A^* < A_c^*$
p_{13}	Decreasing slope of C_{lv} w.r.t. A^* for $A^* > A_c^*$

The added mass term, C_{my} is a univariate function of reduced frequency. having three regions of constant C_{my} separated by linear transitions with smoothed corners. Examples of C_m are shown in the leftmost column of Fig. B.13. The lift coefficient is computed as a piecewise linear function of A^* with zero-intercept $C_{lv,0}$ and critical amplitude A_c^* indicating the transition from increasing to decreases given as smoothed piecewise linear functions of f_r. Examples of $C_{lv,0}$, A_c^*, and C_{lv} are shown in the second, third, and fourth columns of Fig. B.13. The top row shows the single peak variant, and the double peak variant is shown in the bottom row. The following two subsections describe in more detail the computation of each quantity shown in Fig. B.13.

B.1. Single peak parametrization

We begin with a description of the single peak parametrization. We will use the standard notation s_w to denote the soft-plus function with learned characteristic width $w = p_{14}$ The added mass coefficient is given by,

$$\begin{aligned} C_m = p_{10} + m_1(s_w(f - p_2) - s_w(f - p_3)) \\ + m_2(s_w(f - p_4) - s_w(f - p_5)) \end{aligned} \tag{B.2}$$

where,

$$m_1 = \frac{p_{11} - p_{10}}{p_3 - p_2} \quad \text{and} \quad m_2 = \frac{1 - p_{11}}{p_5 - p_4}. \tag{B.3}$$

The values of $C_{lv,0}$ and A_c^* are given by,

$$\begin{aligned} C_{lv,0} = m_3(s_w(f - p_1) - s_w(f - p_2)) + m_4(s_w(f - p_2) \\ - s_w(f - p_3)) + m_5(s_w(f - p_3) - s_w(f - p_4)) \end{aligned} \tag{B.4}$$

and

$$\begin{aligned} A_c^* = m_6(s_w(f - p_1) - s_w(f - p_2)) + m_7(s_w(f - p_2) \\ - s_w(f - p_3)) + m_8(s_w(f - p_3) - s_w(f - p_4)), \end{aligned} \tag{B.5}$$

Table B.5
Description and bounds of parameters for hydrodynamic coefficients in single peak parametrization.

p_1	$(0.08, 0.35)$	p_6	$(0, 0.5)$	p_{11}	$(1, 10)$
p_2	$(p_1, 0.35)$	p_7	$(0, 0.5)$	p_{12}	$(0.1, 5)$
p_3	$(p_2, 0.35)$	p_8	$(0, 2)$	p_{13}	$(1, 5)$
p_4	$(p_3, 0.35)$	p_9	$(0, 2)$	p_{14}	$(10^{-5}, 0.005)$
p_5	$(p_4, 0.35)$	p_{10}	$(-2, 1)$		

where

$$\begin{aligned} m_3 &= \frac{p_6}{p_2 - p_1} & m_6 &= \frac{p_8}{p_2 - p_1} \\ m_4 &= \frac{p_7 - p_6}{p_3 - p_2} & m_7 &= \frac{p_9 - p_8}{p_3 - p_2} \\ m_5 &= \frac{-p_7}{p_4 - p_3} & m_8 &= \frac{-p_9}{p_4 - p_3} \end{aligned} \tag{B.6}$$

The lift coefficient is given by,

$$C_{lv} = \begin{cases} C_{lv,0} + A^* p_{12}, & \text{if } A^* \leq A_c^* \\ C_{lv,0} + A_c^* p_{12} - (A^* - A_c^*) p_{13}, & \text{if } A^* > A_c^* \end{cases} \tag{B.7}$$

Each variable is bounded based on the intervals described in Table B.5. Open boundaries are enforced through fitting the transformed variables $q_i = \sigma^{-1}((p_i - p_{min})/(p_{max} - p_{min}))$ where p_{min} and p_{max} are the bounds for the given parameter and σ is the sigmoid function, which smoothly transforms $\mathbb{R}$ into $(0, 1)$.

B.2. Double peak parametrization

The double peak parametrization differs in the representation of $C_{lv,0}$ and A_c^*, as well as having different reduced frequencies for C_m. The added mass coefficient is given by,

$$\begin{aligned} C_m &= p_{15} + m_1(s_w(f - p_2) - s_w(f - p_6)) \\ &\quad + m_2(s_w(f - p_7) - s_w(f - p_8)) \end{aligned} \tag{B.8}$$

where,

$$m_1 = \frac{p_{16} - p_{15}}{p_7 - p_2} \quad \text{and} \quad m_2 = \frac{1 - p_{16}}{p_8 - p_7}. \tag{B.9}$$

The values of $C_{lv,0}$ and A_c^* are given by,

$$\begin{aligned} C_{lv,0} &= m_3(s_w(f - p_1) - s_w(f - p_2)) \\ &\quad + m_4(s_w(f - p_2) - s_w(f - p_3)) \\ &\quad + m_5(s_w(f - p_3) - s_w(f - p_4)) \\ &\quad + m_6(s_w(f - p_4) - s_w(f - p_5)), \end{aligned} \tag{B.10}$$

and

$$\begin{aligned} A_c^* &= m_7(s_w(f - p_1) - s_w(f - p_2)) \\ &\quad + m_8(s_w(f - p_2) - s_w(f - p_3)) \\ &\quad + m_9(s_w(f - p_3) - s_w(f - p_4)) \\ &\quad + m_{10}(s_w(f - p_4) - s_w(f - p_5)), \end{aligned} \tag{B.11}$$

where

$$\begin{aligned} m_3 &= \frac{p_9}{p_2 - p_1} & m_7 &= \frac{p_{12}}{p_2 - p_1} \\ m_4 &= \frac{p_{10} - p_9}{p_3 - p_2} & m_8 &= \frac{p_{13} - p_{12}}{p_3 - p_2} \\ m_5 &= \frac{p_{11} - p_{10}}{p_4 - p_3} & m_9 &= \frac{p_{14} - p_{13}}{p_4 - p_3} \\ m_6 &= \frac{-p_{11}}{p_5 - p_4} & m_{10} &= \frac{-p_{14}}{p_5 - p_4} \end{aligned} \tag{B.12}$$

Table B.6
Description and bounds of parameters for hydrodynamic coefficients in double peak parametrization.

p_1	$(0.08, 0.35)$	p_6	$(0.08, 0.35)$	p_{11}	$(0.08, 0.35)$	p_{16}	$(0.08, 0.35)$
p_2	$(0.08, 0.35)$	p_7	$(0.08, 0.35)$	p_{12}	$(0.08, 0.35)$	p_{17}	$(0.08, 0.35)$
p_3	$(0.08, 0.35)$	p_8	$(0.08, 0.35)$	p_{13}	$(0.08, 0.35)$	p_{18}	$(0.08, 0.35)$
p_4	$(0.08, 0.35)$	p_9	$(0.08, 0.35)$	p_{14}	$(0.08, 0.35)$	p_{19}	$(0.08, 0.35)$
p_5	$(0.08, 0.35)$	p_{10}	$(0.08, 0.35)$	p_{15}	$(0.08, 0.35)$		

The lift coefficient is given by,

$$C_{lv} = \begin{cases} C_{lv,0} + A^* p_{17}, & \text{if } A^* \leq A_c^* \\ C_{lv,0} + A_c^* p_{17} - (A^* - A_c^*) p_{18}, & \text{if } A^* > A_c^* \end{cases} \tag{B.13}$$

Bounds for each variable are shown in Table B.6

Appendix C. Solution to Eq. (8)

The inner loop of the optimization procedure for the rigid cylinder case requires determining roots of the two error terms given by,

$$\begin{aligned} \text{frequency error} &= \left| \hat{f}_r^{-1} - U_r \sqrt{\frac{m^* + C_{my}(\hat{f}_r; \mathbf{p})}{m^* + 1}} \right| \\ \text{amplitude error} &= \left| \hat{A}^* - \frac{C_{lv}(\hat{f}_r, \hat{A}^*; \mathbf{p}) U_r^2}{4\pi^3 (m^* + 1)\zeta} \right|. \end{aligned} \tag{C.1}$$

for each datapoint. We first show that for any $\hat{f}_r$ there exists $\hat{A}^*$ such that the amplitude error is zero. Note that for fixed $\hat{f}_r$ we compute C_{lv} as,

$$C_{lv}(\hat{A}^*) = \begin{cases} C_{lv,0} + A^* p_{12}, & \text{if } A^* \leq A_c^* \\ C_{lv,0} + A^* p_{12} - (A^* - A_c^*) p_{13}, & \text{if } A^* > A_c^* \end{cases} \tag{C.2}$$

If $C_{lv,0}(\hat{f}_r) = 0$ then $C_{lv}(\hat{A}^*, \hat{f}_r) \leq 0$ for all $\hat{A}^*$ with equality at $\hat{A}^* = 0$, hence $\hat{A}^* = 0$ uniquely sets the amplitude error to zero. Now consider $C_{lv,0}(\hat{f}_r) > 0$. The function of $\hat{A}^*$ inside the absolute value is convex, tends to positive infinity, since C_{lv} is decreasing for large $\hat{A}^*$, and has negative intercept at $\hat{A}^* = 0$. Then the unique value of $\hat{A}^*$ which sets the amplitude error to zero is given by,

$$\hat{A}^* = \begin{cases} \dfrac{C_{lv,0}}{B^{-1} - \alpha}, & \text{if } BC_{lv.c} \leq A_c^* \\ \dfrac{C_{lv,c} + \beta A_c^*}{B^{-1} + \beta}, & \text{otherwise,} \end{cases} \tag{C.3}$$

where,

$$B = \frac{U_r^2}{4\pi^3 (m^* + 1)\zeta} \tag{C.4}$$

$$C_{lv,c} = C_{lv,0} + \alpha A_c^*, \tag{C.5}$$

and α and β are p_{12} and p_{13}.

The frequency error terms have at least one root. Let,

$$\phi(\hat{f}_r) = U_r \sqrt{\frac{m^* + C_{my}(\hat{f}_r; \mathbf{p})}{m^* + 1}}. \tag{C.6}$$

Note that ϕ is finite and that $\lim_{\hat{f}_r \to \infty} \phi = U_r$ while $\hat{f}_r^{-1}$ is continuous and monotonically decreasing on $(0, \infty)$. For $U_r \neq 0$ we are therefore guaranteed an odd number of solutions. Since we consider values of $\hat{f}_r$ on a bounded interval $f\hat{f}_r \in [f_{r,min}, f_{r,max}]$ it is plausible that all values of $\hat{f}_r$ that set the frequency error to zero will be outside. This was observed only for poor initial conditions and did not have an effect on late stages of the optimization. We solve for $\hat{f}_r$ using bisection, which allows us to find the minimal $\hat{f}_r$ satisfying zero frequency error to within a specified tolerance.

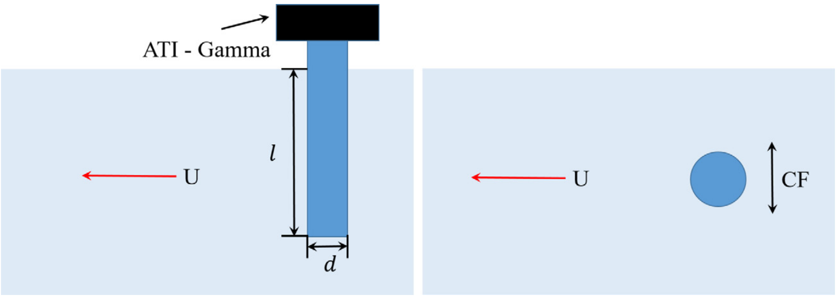

(a) (b)

Fig. E.14. A sketch of the rigid cylinder forced vibration experimental setup: (a) side view; (b) top view.

Appendix D. Optimization pseudocode

The pseudocode for the algorithm used for problems (9) and (12) is given by Alg. 1. Note that optimization is performed in the transformed variables $\mathbf{q}$ rather than $\mathbf{p}$, as explained in the previous section. To avoid superfluous notation, we use $J_r(\mathbf{q})$ to be $J(\mathbf{p}(\mathbf{q})) + \mathcal{R}(\mathbf{p}(\mathbf{q}))$.

Algorithm 1 Stochastic Coordinate Descent($J_r, \mathbf{q}_0$)

```
Initialize $\mathbf{q}$
for $i = 1, \ldots, n_{iters}$:
    Select $\mathbf{V} \in \mathbb{R}^{d \times d}$ with $\mathbf{V}^T\mathbf{V} = \mathbf{I}_d$
    for $j = 1, \ldots, d$ :
        $E = \{\epsilon_k\}_{k=1}^{n_{samp}}$, with $\epsilon_k \sim p_\epsilon^{(i)}$
        $k_{best} = \underset{k}{arg\,min} J_r(\mathbf{q} + \epsilon_k \mathbf{v}_j)$
        if $J_r(\mathbf{q} + \epsilon_k \mathbf{v}_j) < J_r(\mathbf{q})$ then $\mathbf{q} = \mathbf{q} + \epsilon_k \mathbf{v}_j$
return $\mathbf{q}$
```

In our work $\mathbf{V}$ is selected to alternate between the identity matrix with randomly permuted columns and a random unitary matrix. This allows the algorithm to fine tune individual parameters, when the identity is used, but does not constrain it to those descent directions. The sampling distribution $p_\epsilon^{(i)}$ is set the unit normal for the first 20, for rigid, or 10, for flexible cylinder, problems before allowing the variance to decay geometrically. The number of samples, n_{samp} was set to 16 for rigid cylinder cases and 8 for flexible cylinder cases. In some cases the algorithm becomes stuck in a local minimum. This is prevalent when the initial estimate of $\mathbf{q}$, which we sampled randomly, yields an added mass model that set all frequency estimates to the lowest value possible. We avoid this by sampling many initial conditions, running a single step of Alg. 1, and continuing with only those conditions with the lowest error.

The initial value of $\mathbf{q}$ is found via taking a number of random samples and selecting the parameter vector with lowest error. For rigid cylinder cases where the low cost of the computational problem allowed for more restarts, initial estimates were given by the best third of a pool of three times the number of optimizer restarts. A single step of the coordinate descent algorithm was also applied to each initial guess prior to evaluation. For the flexible cylinder example, each initial guess was taken as the best of 25 random initial $\mathbf{q}$ vectors. The sampling distribution for all cases was the standard multivariate normal.

Appendix E. Rigid cylinder forced vibration

The experimental setup for the rigid cylinder forced vibration is shown in Fig. E.14. The rigid cylinder model is mounted on the carriage of the MIT Sea Grant Intelligent Towing Tank (ITT), piercing through the water. The cylinder diameter is $D = 3.81$ cm (1.5") and in-water length is $L = 45.72$ cm (18"). The cylinder is made from hard anodized aluminum tube to prevent corrosion when staying in the water for long periods of time, as required by the ITT automated experimental process. A 6-axis ATI-Gamma force sensor is mounted on top of the cylinder and out of the water, measuring the forces on the cylinder at 1000 Hz, and at the same time, while simultaneously recording the cylinder prescribed motion to calculate accurately the hydrodynamic coefficients. A detailed description of the setup can be found in Fan et al. (2019a).

The cylinder is towed at various velocities U, resulting in Re that ranges from 2,000 to 19,000. The cylinder's prescribed motion is as follows,

$$Y(t) = Y_0 \cos(2\pi f_0 t), \tag{E.1}$$

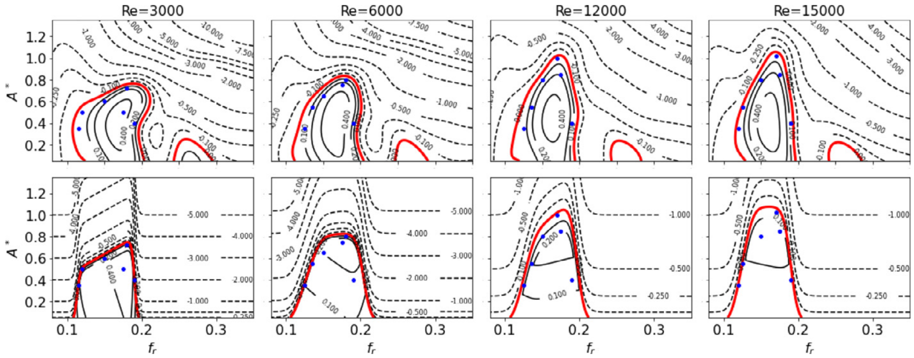

Fig. E.15. C_{lv} comparison between GPR (top row) and VIVopt database using 4 samples (bottom row) at $Re = 3,000$ (first column), $Re = 8,000$ (second column), $Re =$ 12,000 (third column), and $Re =$ 15,000 (fourth column). Blue dots show the location of the samples.

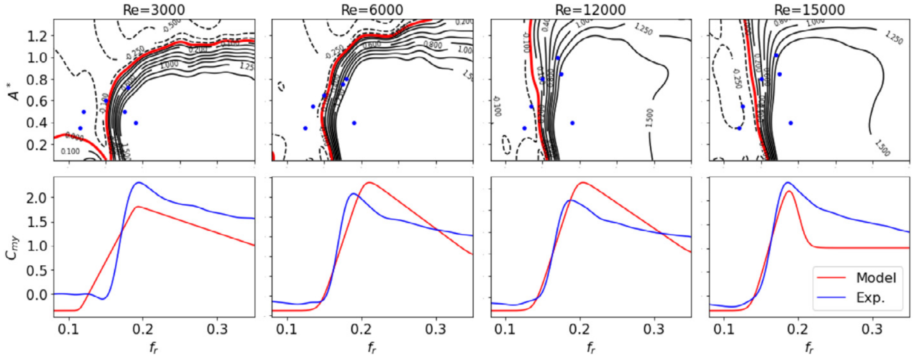

Fig. E.16. C_{my} comparison between GPR (top row) and parametric database using 4 samples (bottom row) at $Re = 3,000$ (first column), $Re = 8,000$ (second column), $Re =$ 12,000 (third column), and $Re =$ 15,000 (fourth column). Blue dots show the location of the samples.

where Y_0 and f_0 are the cross-flow oscillation amplitude and frequency, respectively. The lift and drag forces on the cylinder are modeled as follows,

$$\begin{aligned} L(t) &= L_0 \cos(2\pi f_0 t + \phi_0), \\ D(t) &= D_m + \widetilde{D}(t), \end{aligned} \tag{E.2}$$

where D_m is the magnitude of the mean drag force, $\widetilde{D}$ is the oscillating drag forces, L_0 is the magnitude of the oscillating lift forces at frequency f_0, and ϕ_0 is the phase difference between the cross-flow motion and the oscillatory lift force. The hydrodynamic coefficients, viz., the mean drag coefficient C_d, lift coefficient in phase with velocity C_{lv}, and added mass coefficient in the cross-flow direction C_{my}, are functions of the non-dimensional cross-flow amplitude $\frac{A_y}{D} = \frac{Y_0}{D}$, the reduced frequency $f_r = \frac{f_0 D}{U}$, and Re. From the experimental data, we can calculate the three hydrodynamic coefficients as follows,

$$\begin{aligned} C_d &= \frac{2D_m}{\rho_f l d U^2}, \\ C_{lv} &= \frac{2L_0 \sin(\phi_0)}{\rho_f l D U^2}, \\ C_{my} &= \frac{L_0 \cos(\phi_0)}{2\pi \rho_f \forall Y_0 f_0}, \end{aligned} \tag{E.3}$$

where ρ_f is the fluid density and $\forall$ is the cylinder fluid displacement, $\forall = \frac{\pi}{4} D^2 l$.

To reduced the large number of experimental runs required, instead of systematic grid testing, an adaptive sampling strategy is applied based on Guassian process regression (GPR) (Rasmussen, 2003).

To validate the current functional representation of hydrodynamic coefficients and the use of learning methods, several Re cases have been selected. In the current paper, we use only 4 hand-picking sampling points to learn the C_{lv} and C_{my}

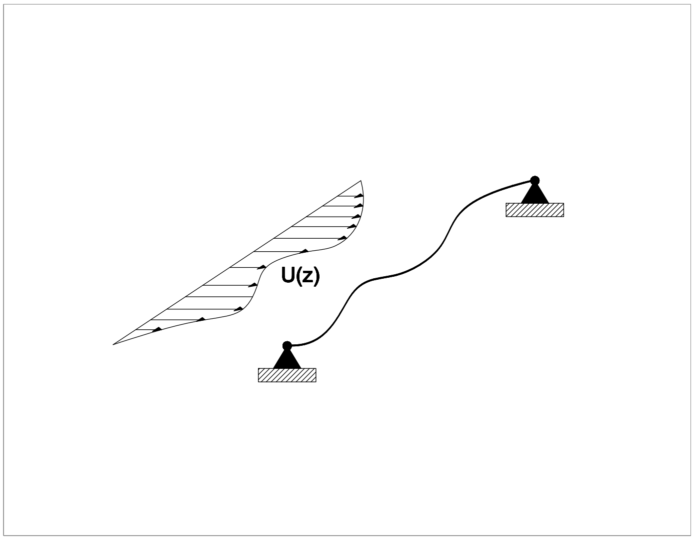

Fig. F.17. Flexible riser within a non-uniform flow profile.

optimal parameters for several *Re* cases (samples close to $C_{lv} = 0$ are selected for C_{lv}, and both positive and negative C_{my} regions are probed twice.). The comparison between the GPR and VIVopt results for C_{lv} and C_{my} are plotted in Fig. E.15 and Fig. E.16. Fig. E.15 shows for the C_{lv} that the parametric results with learned optimal parameters can capture the large positive region around $f_r = 0.15$ and successfully describe the trend of increasing maximum A^* with increasing *Re*. Furthermore, the first row of Fig. E.16 presents the GPR results for C_{my} versus *Re* at different *Re*, showing that C_{my} has similar trends as function of f_r and A^*. C_{my} changes drastically from a negative to a large positive value around $f_r = 0.16$; previous research has shown using flow visualization that such changes are due to a wake mode change from a "2P" pattern to a "2S" pattern (Carberry et al., 2005). The second row of Fig. E.16 shows that the parametric database results with learned optimal parameters match well the average C_{my} provided by GPR over various A^*s. It is found that GPR and FR results for C_{my} match better at higher *Re*, because C_{my} have weaker dependence on A^* at higher *Re*.

Appendix F. Norwegian deepwater programme (NDP) riser motion reconstruction

We proceed to analyze data for flexible riser models depicted schematically in Fig. F.17. Experimental data from the Norwegian Deepwater Programme (NDP) has been used to test the optimization algorithms presented in this paper. The experiments were performed by NDP in the MARINTEK Offshore Basin on bare high length-to-diameter ratio (L/D) risers. The experimental data was collected by micro-bending strain and acceleration sensors along the riser, in both the In-Line (IL) and Cross-FLow (CF) directions. The bare riser used in these experiments has length $L_{Riser} = 38$ m and outer diameter $D_{Riser} = 27$ mm. The number of transducers recording accelerations and bending moments vary in the IL and CF directions:

Type	Cross-flow	In-line
Bending strains	40	24
Accelerations	8	8

A complex post-processing framework is adopted to calculate the time-varying deformed shape of the riser, which we describe herein (see Fig. F.17).The difficulty in reconstructing the deformed shape is that we rely on a number of strain and acceleration measurements at discrete points along the riser (Mukundan, 2008). Here we describe the formulation only for CF displacements, because IL displacements were treated in the same manner. Given that the ends of the riser are fixed, we can use the following Fourier expansion to represent the deformed shape.

$$y(z,t) = \sum_{n=0}^{\infty} w_n(t)\varphi_n(z) \tag{F.1}$$

$$\varphi_n(z) = \sin(n\pi z/L) \tag{F.2}$$

First, we relate measured bending strains ε the local curvature κ.

$$\kappa = \varepsilon / R \tag{F.3}$$

Truncating at an appropriate number of modes N:

$$\kappa(z,t) = \sum_{n=1}^{N} w_n(t)\varphi_n''(z) \quad , \quad a(z,t) = \sum_{n=1}^{N} w_{n_{tt}}(t)\varphi_n(z) \tag{F.4}$$

$$\varphi_n(z) = \sin(n\pi z/L) \Rightarrow \varphi''(z) = -(n\pi/L)^2 \sin(n\pi z/L) \tag{F.5}$$

We exploit the fact that the measurements are sampled at high frequency in time by using the following Fourier transforms:

$$\mathcal{F}\{w_n(t)\} = \hat{w}_n(\omega) \tag{F.6}$$

$$\mathcal{F}\{y(z,t)\} = \hat{y}(z,\omega) \tag{F.7}$$

$$\mathcal{F}\{a(z,t)\} = \hat{a}(z,\omega) \tag{F.8}$$

$$\mathcal{F}\{\kappa(z,t)\} = \hat{\kappa}(z,\omega) \tag{F.9}$$

From which we can obtain:

$$\hat{y}(z,\omega) = \sum_{n=1}^{N} \hat{w}_n(\omega)\phi_n(z) \tag{F.10}$$

$$\hat{a}(z,\omega) = -\omega^2 \hat{y}(z,\omega) = -\omega^2 \sum_{n=1}^{N} \hat{w}_n(\omega)\phi_n(z) \tag{F.11}$$

$$\hat{\kappa}(z,\omega) = \sum_{n=1}^{N} \hat{w}_n(\omega)\phi_{n_{zz}}(z) \tag{F.12}$$

Expressing the problem in the frequency domain allows expressing the previous three equations in matrix form as shown below:

$$\Phi \hat{W} = \hat{Y}, \tag{F.13}$$

where,

$$\hat{W} = \begin{bmatrix} \hat{w}_1(\omega_1) & \hat{w}_1(\omega_2) & \dots & \hat{w}_1(\omega_\Lambda) \\ \hat{w}_2(\omega_1) & \hat{w}_2(\omega_2) & \dots & \hat{w}_2(\omega_\Lambda) \\ \hat{w}_3(\omega_1) & \hat{w}_3(\omega_2) & \dots & \hat{w}_3(\omega_\Lambda) \\ \vdots & \vdots & \ddots & \vdots \\ \hat{w}_N(\omega_1) & \hat{w}_N(\omega_2) & \dots & \hat{w}_N(\omega_\Lambda) \end{bmatrix}, \tag{F.14}$$

$$\Phi = \begin{bmatrix} \Phi_1(z_1) & \Phi_2(z_1) & \dots & \Phi_N(z_1) \\ \Phi_1(z_2) & \Phi_2(z_2) & \dots & \Phi_N(z_2) \\ \Phi_1(z_3) & \Phi_2(z_3) & \dots & \Phi_N(z_3) \\ \vdots & \vdots & \ddots & \vdots \\ \Phi_1\left(z_{M_y}\right) & \Phi_2\left(z_{M_y}\right) & \dots & \Phi_N\left(z_{M_y}\right) \\ \Phi_1''(z_1) & \Phi_2''(z_1) & \dots & \Phi_N''(z_1) \\ \Phi_1''(z_2) & \Phi_2''(z_2) & \dots & \Phi_N''(z_2) \\ \Phi_1''(z_3) & \Phi_2''(z_3) & \dots & \Phi_N''(z_3) \\ \vdots & \vdots & \ddots & \vdots \\ \Phi_1''\left(z_{M_k}\right) & \Phi_2''\left(z_{M_k}\right) & \dots & \Phi_N''\left(z_{M_k}\right) \end{bmatrix}, \tag{F.15}$$

$$\hat{Y}=\begin{bmatrix}
\hat{y}\left(z_1,\omega_1\right) & \hat{y}\left(z_1,\omega_2\right) & \dots & \hat{y}\left(z_1,\omega_\Lambda\right)\\
\hat{y}\left(z_2,\omega_1\right) & \hat{y}\left(z_2,\omega_2\right) & \cdots & \hat{y}\left(z_2,\omega_\Lambda\right)\\
\hat{y}\left(z_3,\omega_1\right) & \hat{y}\left(z_3,\omega_2\right) & \cdots & \hat{y}\left(z_3,\omega_\Lambda\right)\\
\vdots & \vdots & \ddots & \vdots\\
\hat{y}\left(z_{M_y},\omega_1\right) & \hat{y}\left(z_{M_y},\omega_2\right) & \cdots & \hat{y}\left(z_{M_y},\omega_\Lambda\right)\\
\frac{-\hat{a}(z_1,\omega_1)}{\omega_1^2} & \frac{-\hat{a}(z_1,\omega_2)}{\omega_2^2} & \cdots & \frac{-\hat{a}(z_1,\omega_\Lambda)}{\omega_\Lambda^2}\\
\frac{-\hat{a}(z_2,\omega_1)}{\omega_1^2} & \frac{-\hat{a}(z_2,\omega_2)}{\omega_2^2} & \cdots & \frac{-\hat{a}(z_2,\omega_\Lambda)}{\omega_\Lambda^2}\\
\frac{-\hat{a}(z_3,\omega_1)}{\omega_1^2} & \frac{-\hat{a}(z_3,\omega_2)}{\omega_2^2} & \cdots & \frac{-\hat{a}(z_3,\omega_\Lambda)}{\omega_\Lambda^2}\\
\vdots & \vdots & \ddots & \vdots\\
\frac{-\hat{a}\left(z_{M_a},\omega_1\right)}{\omega_1^2} & \frac{-\hat{a}\left(z_{M_a},\omega_2\right)}{\omega_2^2} & \cdots & \frac{-\hat{a}\left(z_{M_a},\omega_\Lambda\right)}{\omega_\Lambda^2}\\
\hat{\kappa}\left(z_1,\omega_1\right) & \hat{\kappa}\left(z_1,\omega_2\right) & \cdots & \hat{\kappa}\left(z_1,\omega_\Lambda\right)\\
\hat{\kappa}\left(z_2,\omega_1\right) & \hat{\kappa}\left(z_2,\omega_2\right) & \cdots & \hat{\kappa}\left(z_2,\omega_\Lambda\right)\\
\hat{\kappa}\left(z_3,\omega_1\right) & \hat{\kappa}\left(z_3,\omega_2\right) & \cdots & \hat{\kappa}\left(z_3,\omega_\Lambda\right)\\
\vdots & \vdots & \ddots & \vdots\\
\hat{\kappa}\left(z_{M_k},\omega_1\right) & \hat{\kappa}\left(z_{M_k},\omega_2\right) & \cdots & \hat{\kappa}\left(z_{M_k},\omega_\Lambda\right)
\end{bmatrix}. \tag{F.16}$$

We solve for each value of ω using the pseudo-inverse Φ^+.

$$\hat{w}=\Phi^+\hat{Y} \tag{F.17}$$

Taking the inverse Fourier transform of $\hat{w}$, we find the coefficient matrix in the time domain, and the riser CF displacement is found:

$$y(z,t)=\sum_{n=0}^{N} w_n(t)\varphi_n(z) \tag{F.18}$$

Finding high order modes in (F.13) requires a minimum number of sensors . Furthermore the use of the pseudo-inverse Φ^+ is equivalent to a least-squares fit in the frequency domain. Therefore the number of sensors available will limit the number of modes N we can use.

To improve the quality of reconstruction, we employed band-pass filtering to remove low and high frequency noise. used different weighting for the strain and acceleration measurements; and set to zero the terms $\phi_N''(z_{Mk})$ for all N below a threshold value $N <= N_{low}$ the robustness.

References

Aronsen, K.H., 2007. An Experimental Investigation of In-Line and Combined In-Line and Cross-Flow Vortex Induced Vibrations (Ph.D. thesis). Norwegian University of Science and Technology.

Bearman, P.W., 2011. Circular cylinder wakes and vortex-induced vibrations. J. Fluids Struct. 27 (5–6), 648–658.

Bourguet, R., Modarres-Sadeghi, Y., Karniadakis, G.E., et al., 2011. Wake-body resonance of long flexible structures is dominated by counterclockwise orbits. Phys. Rev. Lett. 107 (13), 134502.

Braaten, H., Lie, H., 2004. Technical Report, (512394.00), Norwegian Marine Technology Research Institute, p. 01.

Carberry, J., Sheridan, J., Rockwell, D., 2005. Controlled oscillations of a cylinder: forces and wake modes. J. Fluid Mech. 538, 31–69.

Chang, C.C.J., Kumar, R.A., Bernitsas, M.M., 2011. VIV and galloping of single circular cylinder with surface roughness at 3.0× 104< Re <1.2× 105. Ocean Engineering 38 (16), 1713–1732.

Chen, Y., Fu, S., Xu, Y., et al., 2013. Hydrodynamic characters of a near-wall circular cylinder oscillating in cross flow direction in steady current. Acta Phys. Sin. 62 (6), 064701.

Dahl, J., Hover, F., Triantafyllou, M., Oakley, O., 2010. Dual resonance in vortex-induced vibrations at subcritical and supercritical Reynolds numbers. J. Fluid Mech. 643, 395.

Ding, Z., Balasubramanian, S., Lokken, R., et al., 2004. Lift and damping characteristics of bare and straked cylinders at riser scale Reynolds numbers. In: Offshore Technology Conference.

Fan, D., 2019. Mapping the Hydrodynamic Properties of Flexible and Rigid Bodies Undergoing Vortex-Induced Vibrations (Ph.D. thesis). Massachusetts Institute of Technology.

Fan, D., Jodin, G., Consi, T., et al., 2019a. A robotic Intelligent Towing Tank for learning complex fluid-structure dynamics. Science Robotics 4 (36).

Fan, D., Triantafyllou, M.S., 2017. Vortex induced vibration of riser with low span to diameter ratio buoyancy modules. In: The 27th International Ocean and Polar Engineering Conference. International Society of Offshore and Polar Engineers.

Fan, D., Wang, Z., Triantafyllou, M., et al., 2019b. Mapping the properties of the vortex-induced vibrations of flexible cylinders in uniform oncoming flow. J. Fluid Mech. 881, 815–858.

Gabbai, R., Benaroya, H., 2005. An overview of modeling and experiments of vortex-induced vibration of circular cylinders. J. Sound Vib. 282 (3–5), 575–616.

Gao, F., Han, L., 2012. Implementing the Nelder-Mead simplex algorithm with adaptive parameters. Comput. Optim. Appl. 51 (1), 259–277.

Gopalkrishnan, R., 1993. Vortex-Induced Forces on Oscillating Bluff Cylinders (Ph.D. thesis). Massachusetts Institute of Technology.

Govardhan, R., Williamson, C., 2006. Defining the'modified Griffin plot'in vortex-induced vibration: revealing the effect of Reynolds number using controlled damping. J. Fluid Mech. 561, 147.

Han, Q., Ma, Y., Xu, W., et al., 2018. Hydrodynamic characteristics of an inclined slender flexible cylinder subjected to vortex-induced vibration. Int. J. Mech. Sci. 148, 352–365.

Hover, F., Miller, S., Triantafyllou, M., 1997. Vortex-induced vibration of marine cables: experiments using force feedback. J. Fluids Struct. 11 (3), 307–326.

Hover, F., Techet, A., Triantafyllou, M., 1998. Forces on oscillating uniform and tapered cylinders in a crossflow. Cambridge University Press.

Jauvtis, N., Williamson, C.H.K., 2003. Vortex-induced vibration of a cylinder with two degrees of freedom. J. Fluids Struct. 17 (7), 1035–1042.

Kirkpatrick, S., Gelatt, C.D., Vecchi, M.P., 1983. Optimization by simulated annealing. Science 220 (4598), 671–680.

Klamo, J., Leonard, A., Roshko, A., 2005. On the maximum amplitude for a freely vibrating cylinder in cross-flow. J. Fluids Struct. 21 (4), 429–434.

Larsen, C.M., Vikestad, K., Yttervik, R., et al., 2001. VIVANA Theory Manual. Marintek, Trondheim, Norway.

Le Garrec, J., Fan, D., Wu, B., Triantafyllou, M.S., 2016. Experimental investigation of cross flow-inline coupled vortex-induced vibration on riser with finite length buoyancy module. In: OCEANS 2016 MTS/IEEE Monterey. IEEE, pp. 1–7.

Lee, J., Bernitsas, M., 2011. High-damping, high-Reynolds VIV tests for energy harnessing using the VIVACE converter. Ocean Eng. 38 (16), 1697–1712.

Lie, H., Braaten, H., Szwalek, J., et al., 2013. Drilling riser VIV tests with prototype Reynolds numbers. In: ASME 2013 32nd International Conference on Ocean, Offshore and Arctic Engineering. American Society of Mechanical Engineers Digital Collection.

Lin, K., Fan, D., Wang, J., 2020. Dynamic response and hydrodynamic coefficients of a cylinder oscillating in crossflow with an upstream wake interference. Ocean Eng. 209, 107520.

Lucor, D., Su, C.-H., Karniadakis, G.E., 2004. Generalized polynomial chaos and random oscillators. Internat. J. Numer. Methods Engrg. 60 (3), 571–596.

Martins, F., Avila, J., 2019. Effects of the Reynolds number and structural damping on vortex-induced vibrations of elastically-mounted rigid cylinder. Int. J. Mech. Sci. 156, 235–249.

Meng, X., Wang, Z., Fan, D., Triantafyllou, M., Karniadakis, G.E., 2020. A fast multi-fidelity method with uncertainty quantification for complex data correlations: Application to vortex-induced vibrations of marine risers. arXiv preprint arXiv:2012.13481.

Modarres-Sadeghi, Y., Chasparis, F., Triantafyllou, M., Tognarelli, M., Beynet, P., 2011. Chaotic response is a generic feature of vortex-induced vibrations of flexible risers. J. Sound Vib. 330 (11), 2565–2579.

Mukundan, H., 2008. Vortex-Induced Vibration of Marine Risers: Motion and Force Reconstruction from Field and Experimental Data (Ph.D. thesis). Massachusetts Institute of Technology.

Raghavan, K., Bernitsas, M., 2011. Experimental investigation of Reynolds number effect on vortex induced vibration of rigid circular cylinder on elastic supports. Ocean Eng. 38 (5–6), 719–731.

Rasmussen, C.E., 2003. Gaussian processes in machine learning. In: Summer School on Machine Learning. Springer, pp. 63–71.

Roveri, F.E., Vandiver, J.K., 2001. Using Shear7 for assessment of fatigue damage caused by current induced vibrations. In: Proc. 20th OMAE Conf. pp. 3–8.

Rudy, S., Fan, D., Ferrandis, J.d.A., Sapsis, T., Triantafyllou, M.S., 2021. Learning optimal parametric hydrodynamic database for vortex-induced crossflow vibration prediction of both freely-mounted rigid and flexible cylinders. In: The 31st International Ocean and Polar Engineering Conference. OnePetro.

Sarpkaya, T., 1978. Fluid Forces on Oscillating Cylinders. NASA STI/Recon Technical Report A, 78, pp. 275–290.

Smogeli, O.A.y.N., Hover, F.S., Triantafyllou, M.S., 2003. Force-feedback control in VIV experiments. In: International Conference on Offshore Mechanics and Arctic Engineering. Vol. 36835, pp. 685–695.

Triantafyllou, M., Triantafyllou, G., Tein, Y., et al., 1999. Pragmatic riser VIV analysis. In: Offshore Technology Conference.

Vikestad, K., 1998. Multi-Frequency Response of a Cylinder Subjected to Vortex Shedding and Support Motions (Ph.D. thesis). Norwegian University of Science and Technology Trondheim.

Wang, J., Fan, D., Lin, K., 2020a. A review on flow-induced vibration of offshore circular cylinders. J. Hydrodyn. 32 (3), 415–440.

Wang, Z., Fan, D., Triantafyllou, M.S., et al., 2020b. A large-eddy simulation study on the similarity between free vibrations of a flexible cylinder and forced vibrations of a rigid cylinder. J. Fluid Struct..

Williamson, C.H., 1996. Vortex dynamics in the cylinder wake. Annu. Rev. Fluid Mech. 28 (1), 477–539.

Williamson, C., Govardhan, R., 2004. Vortex-induced vibrations. Annu. Rev. Fluid Mech. 36, 413–455.

Williamson, C.H.K., Govardhan, R., 2008. A brief review of recent results in vortex-induced vibrations. J. Wind Eng. Ind. Aero. 96 (6–7), 713–735.

Wright, S.J., 2015. Coordinate descent algorithms. Math. Program. 151 (1), 3–34.

Wu, B., Le Garrec, J., Fan, D., Triantafyllou, M.S., 2017. Kill line model cross flow inline coupled vortex-induced vibration. In: International Conference on Offshore Mechanics and Arctic Engineering. Vol. 57649, American Society of Mechanical Engineers, p. V002T08A010.

Wu, J., Yin, D., Lie, H., Riemer-Sørensen, S., Sævik, S., Triantafyllou, M., 2020. Improved VIV response prediction using adaptive parameters and data clustering. J. Mar. Sci. Eng. 8 (2), 127.

Xu, Y., Fu, S., Chen, Y., et al., 2013. Experimental investigation on vortex induced forces of oscillating cylinder at high Reynolds number. Ocean Syst. Eng. 3 (3), 167–180.

Zdravkovich, M.M., 1997a. Flow Around Circular Cylinders: Volume 1: Fundamentals. Vol. 1, Oxford University Press.

Zdravkovich, M., 1997b. Flow around circular cylinders; vol. i fundamentals. J. Fluid Mech. 350 (1), 377–378.

Zheng, H., Price, R., Modarres-Sadeghi, Y., Triantafyllou, G.S., Triantafyllou, M.S., 2011. Vortex-induced vibration analysis (VIVA) based on hydrodynamic databases. In: International Conference on Offshore Mechanics and Arctic Engineering. Vol. 44397, pp. 657–663.

Zhu, H., Zhou, D., Bao, Y., Wang, R., et al., 2018. Wake characteristics of stationary catenary risers with different incoming flow directions. Ocean Eng. 167, 142–155.